

# FOURTH- AND HIGHER-ORDER SEMI-LAGRANGIAN FINITE VOLUME METHODS FOR THE TWO-DIMENSIONAL ADVECTION EQUATION ON ARBITRARILY COMPLEX DOMAINS \*

YUNXIA SUN <sup>†</sup>, KAIYI LIANG <sup>‡</sup>, YUKE ZHU <sup>‡</sup>, ZHI LIN <sup>‡</sup>, AND QINGHAI ZHANG <sup>†‡§</sup>

**Abstract.** To numerically solve the two-dimensional advection equation, we propose a family of fourth- and higher-order semi-Lagrangian finite volume (SLFV) methods that feature (1) fourth-, sixth-, and eighth-order convergence rates, (2) applicability to both regular and irregular domains with arbitrarily complex topology and geometry, (3) ease of handling both zero and nonzero source terms, and (4) the same algorithmic steps for both periodic and incoming penetration conditions. Test results confirm the analysis and demonstrate the accuracy, flexibility, robustness, and excellent conditioning of the proposed SLFV method.

**Key words.** the advection equation, semi-Lagrangian methods, finite volume methods, Yin sets, incoming penetration velocity boundary conditions.

**AMS subject classifications.** 35F16, 65M08, 65M25

**1. Introduction.** The advection equation is an important partial differential equation (PDE) utilized across various scientific fields such as meteorology and fluid mixing and transport. This paper focuses on the two-dimensional advection equation

$$\begin{aligned} (1.1a) \quad & \frac{\partial \rho(\mathbf{x}, t)}{\partial t} + \mathbf{u}(\mathbf{x}, t) \cdot \nabla \rho(\mathbf{x}, t) = S(\mathbf{x}, t), & \text{in } \Omega \times [0, T], \\ (1.1b) \quad & \rho(\mathbf{x}, 0) = \rho_{\text{init}}(\mathbf{x}), & \text{in } \bar{\Omega}, \\ (1.1c) \quad & \rho(\mathbf{x}, t) = \rho_{\text{bc}}(\mathbf{x}, t), & \text{on } \Gamma^-, \end{aligned}$$

where  $\mathbf{x}$  is the spatial position,  $t$  the time,  $\rho$  the unknown scalar,  $\Omega \subset \mathbb{R}^2$  a bounded domain (i.e., a bounded Yin set; see [Definition 2.2](#)),  $\partial\Omega$  the domain boundary,  $\bar{\Omega}$  the closure of  $\Omega$ ,  $\rho_{\text{init}}$  the initial condition,  $\rho_{\text{bc}}$  the boundary condition,  $\mathbf{u} : \bar{\Omega} \times [0, T] \rightarrow \mathbb{R}^2$  a velocity field given *a priori*, and  $S(\mathbf{x}, t)$  the source term that is continuous in  $t$  and Lipschitz continuous in  $\mathbf{x}$ . If  $\rho$  is periodic on  $\Omega$ , (1.1c) should be removed from (1.1); otherwise, to ensure the well-posedness of (1.1),  $\rho_{\text{bc}}$  should be specified on a subset  $\Gamma^- \subset \partial\Omega \times (0, T]$  that depends on the sign of  $\mathbf{u}$  along  $\partial\Omega$ ,

$$(1.2) \quad \Gamma^- := \{(\mathbf{x}, t) : \mathbf{x} \in \partial\Omega, t \in (0, T]; \mathbf{u}(\mathbf{x}, t) \cdot \mathbf{n}(\mathbf{x}) < 0\},$$

where  $\mathbf{n}(\mathbf{x})$  is the unit outward normal vector of  $\partial\Omega$ . If  $\Gamma^- \neq \emptyset$ , we call  $\rho_{\text{bc}} : \Gamma^- \rightarrow \mathbb{R}$  an *incoming penetration condition* and  $\Omega$  an *incoming penetration domain* (or simply a *penetration domain*). If  $\Gamma^- = \emptyset$ , (1.1c) drops out from (1.1) without affecting the well-posedness; see the last paragraph of [Subsection 2.1](#) for such an example.

\*Yunxia Sun and Kaiyi Liang are co-first authors with equal contributions.

**Funding:** Q. Zhang was supported by the grant 12272346 from the National Natural Science Foundation of China. Z. Lin was supported by grants 12071429 and 12090020 from the National Natural Science Foundation of China.

<sup>†</sup>College of Mathematics and System Science, Xinjiang University, Urumqi, Xinjiang Prov., 830046 China ([syxmath@163.com](mailto:syxmath@163.com), [qinghai@zju.edu.cn](mailto:qinghai@zju.edu.cn)).

<sup>‡</sup>School of Mathematical Sciences, Zhejiang University, Hangzhou, Zhejiang Prov., 310058, China ([kyliang@zju.edu.cn](mailto:kyliang@zju.edu.cn), [yukezhu0323@126.com](mailto:yukezhu0323@126.com), [linzhi80@zju.edu.cn](mailto:linzhi80@zju.edu.cn), [qinghai@zju.edu.cn](mailto:qinghai@zju.edu.cn)).

<sup>§</sup> Corresponding author. ([qinghai@zju.edu.cn](mailto:qinghai@zju.edu.cn)) Institute of Fundamental and Transdisciplinary Research, Zhejiang University, Hangzhou, Zhejiang Prov., 310058, China.

Numerical algorithms for solving the advection equation can be categorized into Eulerian, Lagrangian, and semi-Lagrangian methods. These methods can be conceptually unified via *the Lagrangian form of the advection equation*,

$$(1.3) \quad \frac{d\rho}{dt} = S(\mathbf{x}, t),$$

which is equivalent to (1.1a) since the material derivative is defined as  $\frac{d}{dt} := \frac{\partial}{\partial t} + \mathbf{u} \cdot \nabla$ . In the extended phase space, integrate (1.3) along a curve  $\gamma : [s_0, s_1] \rightarrow \Omega \times [0, T]$  and we have  $\rho(\mathbf{x}_1, t_1) - \rho(\mathbf{x}_0, t_0) = \int_{\gamma} d\rho = \int_{\gamma} \left( \nabla \rho, \frac{\partial \rho}{\partial t} \right) \cdot (d\mathbf{x}, dt)$ , i.e.,

$$(1.4) \quad \rho(\mathbf{x}_1, t_1) = \rho(\mathbf{x}_0, t_0) + \int_{\gamma} \nabla \rho \cdot (d\mathbf{x} - \mathbf{u} dt) + \int_{\gamma} S dt,$$

which yields a pure Eulerian method if  $\gamma$  is chosen to be time independent and a pure Lagrangian method if  $\gamma$  is an integral curve of (2.1) or the pathline of a Lagrangian particle; see Definition 2.1. Another choice of  $\gamma$  as a combination of stationary curves and particle pathlines leads to the so-called *semi-Lagrangian methods* [34, 32].

The time step size of pure Eulerian methods is constrained by the Courant-Friedrichs-Lewy (CFL) stability condition. On the other hand, the time step size of a pure Lagrangian method can be arbitrarily large, but particle distributions may evolve to be highly non-uniform, which deteriorates accuracy. Semi-Lagrangian methods resolve disadvantages of the two pure methods by employing a regular Cartesian grid for uniform spatial distribution and tracking particles along pathlines to relax the CFL condition; they have proven to be effective in various applications such as weather forecasting [29, 34, 23] and plasma simulations [2, 33, 5, 17, 6, 26].

In semi-Lagrangian methods, the unknown may be point values for finite difference schemes [26, 27, 38, 7, 20] or cell-averaged values for finite volume schemes [12, 16, 3, 1]. In both cases, the solution often needs to be determined from nearby values via a reconstruction technique such as spline interpolation [11], piecewise parabolic method (PPM) [9], cubic interpolation pseudo-particle method (CIP) [36], and essentially non-oscillatory (ENO)/ weighted ENO (WENO) reconstruction [18, 30, 31].

Many semi-Lagrangian methods were originally designed in one dimension; see, e.g., the finite difference scheme in [27] and the finite volume scheme in [16]. Multi-dimensional problems are often decomposed into a series of one-dimensional subproblems via an operator splitting technique such as the second-order Strang splitting [28] and the fourth-order splitting in [24].

Recently, non-splitting semi-Lagrangian schemes are becoming increasingly popular. For example, the consideration of multi-dimensional flux differences leads to a mass conservative semi-Lagrangian finite difference WENO scheme [38], which imposes an additional restriction on the time step size for numerical stability. Another conservative WENO scheme [43] involves constructing a new WENO reconstruction operator and computing the integral over cell preimages. A machine learning-assisted method [8] accelerates traditional schemes by learning the semi-Lagrangian discretization from data, but is unfortunately subject to the stability constraint of the CFL number being less than 2.

Despite their tremendous successes, current semi-Lagrangian methods still have a number of limits. First, most methods are developed for regular domains and it is not clear how to extend them to irregular domains with complex geometry. Second, most methods assume a periodic condition on  $\rho$  and it is not clear how to generalize these methods to penetration domains. Third, although it encourages reuse of simple

algorithms, the operator splitting technique may result in a significant increase of the number of subproblems in multiple dimensions. For a targeting order of accuracy, one may have to re-derive the splitting process, which may impose additional constraints on the time step size.

The above discussions lead to the following questions:

- (Q-1) Can we develop fourth- and higher-order semi-Lagrangian methods that effectively handle both regular and irregular domains with arbitrarily complex topology and geometry?
- (Q-2) Can the new semi-Lagrangian method apply to both periodic domains and penetration domains?
- (Q-3) Is the new semi-Lagrangian method directly applicable to the case of a nonzero source term?
- (Q-4) While semi-Lagrangian methods are free of the CFL constraints, can we prove the fourth- and higher-order convergence rates of the new method?

In this paper, we give positive answers to all above questions by proposing a family of fourth- and higher-order semi-Lagrangian finite volume (SLFV) methods.

The rest of this paper is organized as follows. We set the theoretical context for this work in [Section 2](#), where we prove [Theorem 2.5](#) as the key result for handling irregular domains. In [Section 3](#), we describe our answers to (Q-1,2,3) by elaborating on the SLFV method and its main components. The convergence rates of SLFV are proved in [Section 4](#), answering (Q-4). In [Section 5](#), we perform various tests on SLFV to demonstrate its high-order accuracy, its capability of handling irregular domains with arbitrarily complex topology and geometry, and its generality for periodic/penetration domains and zero/nonzero source terms. Finally, we conclude this work in [Section 6](#) with several research prospects.

**2. The action of flow maps upon Yin sets.** Continua of arbitrarily complex topology and geometry are modeled by Yin sets [\[41\]](#) and the action of flow maps upon Yin sets furnishes the theoretical context of this paper.

**2.1. Flow maps.** The ordinary differential equation (ODE)

$$(2.1) \quad \frac{d\mathbf{x}}{dt} = \mathbf{u}(\mathbf{x}, t)$$

has a unique solution for any given initial time  $t_0$  and position  $\mathbf{p}(t_0)$  if  $\mathbf{u}(\mathbf{x}, t)$  is continuous in time and Lipschitz continuous in space. This uniqueness gives rise to a *flow map*  $\phi : \mathbb{R}^2 \times \mathbb{R} \times \mathbb{R} \rightarrow \mathbb{R}^2$ , which takes the initial time  $t_0$ , the initial position  $\mathbf{p}(t_0)$  of a Lagrangian particle  $\mathbf{p}$ , and the time increment  $\pm k$ , and returns the position of  $\mathbf{p}$  at  $t_0 \pm k$ :

$$(2.2) \quad \phi_{t_0}^{\pm k}(\mathbf{p}) := \mathbf{p}(t_0 \pm k) = \mathbf{p}(t_0) + \int_{t_0}^{t_0 \pm k} \mathbf{u}(\mathbf{p}(t), t) dt.$$

The set  $\{\phi_{t_0}^\sigma : \sigma \in \mathbb{R}\}$  forms a one-parameter group of diffeomorphisms.

**DEFINITION 2.1 (Pathline).** *The pathline of a Lagrangian particle  $\mathbf{p}$  in a time interval  $(t_0, t_0 \pm k)$  is the curve  $\Phi_{t_0}^{\pm k} : (0, k) \rightarrow \mathbb{R}^2$  given by*

$$(2.3) \quad \Phi_{t_0}^{\pm k}(\mathbf{p}) := \{\phi_{t_0}^{\pm \tau}(\mathbf{p}) : \tau \in (0, k)\}.$$

The flow map naturally generalizes to a point set  $\mathcal{P}$ . As a homeomorphism, the flow map preserves key topological features of  $\mathcal{P}$ .

In the particular case of a *no-penetration domain*, i.e.,  $\forall \mathbf{x} \in \partial\Omega, \mathbf{u}(\mathbf{x}) \cdot \mathbf{n}(\mathbf{x}) = 0$ , the flow map sends points in  $\Omega$  to points in  $\Omega$  and thus a no-penetration domain  $\Omega$  contains the pathline of any particle  $\mathbf{p}$  that is initially inside  $\Omega$ .

**2.2. Yin sets and their partitions.** Denote by  $\mathcal{X}$  a topological space and  $\mathcal{P} \subseteq \mathcal{X}$  a subset. The complement, closure and interior of  $\mathcal{P}$  are denoted as  $\mathcal{P}'$ ,  $\overline{\mathcal{P}}$  and  $\mathcal{P}^\circ$ , respectively. The *exterior* of  $\mathcal{P}$  is defined as  $\mathcal{P}^\perp := (\mathcal{P}')^\circ$ .  $\mathcal{P} \subseteq \mathcal{X}$  is *regular open* if  $\mathcal{P} = (\mathcal{P}^\perp)^\perp$ . This regularity condition captures the physical meaningfulness of continua by precluding low-dimensional features such as isolated gaps and points.

A set  $\mathcal{P} \subseteq \mathbb{R}^2$  is *semianalytic* if there exist a finite number of analytic functions  $g_i : \mathbb{R}^2 \rightarrow \mathbb{R}$  such that  $\mathcal{P}$  is in the universe of a finite Boolean algebra formed by the sets  $\{\mathbf{x} \in \mathbb{R}^2 : g_i(\mathbf{x}) \geq 0\}$ . Intuitively, semianalytic sets have piecewise smooth boundary curves.

**DEFINITION 2.2** (Yin space [41]). *A Yin set  $\mathcal{Y} \subseteq \mathbb{R}^2$  is a regular open semianalytic set whose boundary is bounded. The class of all such Yin sets form the Yin space  $\mathbb{Y}$ .*

The boundedness of the boundary of Yin sets leads to

**THEOREM 2.3** (Zhang and Li [41]).  *$(\mathbb{Y}, \cup^{\perp\perp}, \cap, \perp, \emptyset, \mathbb{R}^2)$  is a Boolean algebra, where the regularized union  $\cup^{\perp\perp}$  is given by  $\mathcal{P} \cup^{\perp\perp} \mathcal{Q} := (\mathcal{P} \cup \mathcal{Q})^{\perp\perp}$  for all  $\mathcal{P}, \mathcal{Q} \in \mathbb{Y}$ .*

Efficient algorithms of Boolean operations on Yin sets have been developed in [41] and are employed in this work to cut and merge cells.

The condition of Yin sets being open leads to the conclusion [41, Theorem 3.9] that the boundary  $\partial\mathcal{Y}$  of any connected Yin set  $\mathcal{Y} \neq \emptyset, \mathbb{R}^2$  can be *uniquely* decomposed into a finite set  $\mathcal{J}_{\partial\mathcal{Y}}$  of pairwise almost disjoint Jordan curves.

**THEOREM 2.4.** *Any connected Yin set  $\mathcal{Y} \neq \emptyset, \mathbb{R}^2$  can be uniquely expressed as*

$$(2.4) \quad \mathcal{Y} = \bigcap_{\gamma_j \in \mathcal{J}_{\partial\mathcal{Y}}} \text{int}(\gamma_j),$$

where  $\text{int}(\gamma_j)$  is the complement of  $\gamma_j$  that always lies to the left of the observer who traverses  $\gamma_j$  according to its orientation and  $\mathcal{J}_{\partial\mathcal{Y}}$  must be one of the two types,

$$(2.5) \quad \begin{cases} \mathcal{J}^- = \{\gamma_1^-, \gamma_2^-, \dots, \gamma_{n_-}^-\}, & n_- \geq 1, \\ \mathcal{J}^+ = \{\gamma^+, \gamma_1^-, \gamma_2^-, \dots, \gamma_{n_-}^-\}, & n_- \geq 0, \end{cases}$$

with  $\gamma^+$  being positively oriented and all  $\gamma_j^-$ 's being negatively oriented and pairwise almost disjoint. In the second case, we have  $\gamma_j^- \prec \gamma^+$  for each  $j = 1, 2, \dots, n_-$ , i.e., the bounded complement of each  $\gamma_j^-$  is a subset of the bounded complement of  $\gamma^+$ .

*Proof.* See [41, page 2348].  $\square$

This unique boundary representation extends to all nontrivial Yin sets via appropriately orienting the boundary Jordan curves, i.e., any  $\mathcal{Y} \neq \emptyset, \mathbb{R}^2$  can be *uniquely* expressed [41, Corollary 3.13] as  $\mathcal{Y} = \bigcup_j^{\perp\perp} \bigcap_i \text{int}(\gamma_{j,i})$  where  $j$  is the index of connected components of  $\mathcal{Y}$  and  $\gamma_{j,i}$  the  $i$ th oriented Jordan curve for the  $j$ th component.

Following [15], we approximate oriented Jordan curves by cubic splines. Hereafter  $\mathbb{Y}_c$  denotes the class of all Yin sets whose boundaries consist of cubic splines. It is straightforward to show that  $\mathbb{Y}_c$  is a subspace and a subalgebra of  $\mathbb{Y}$ .

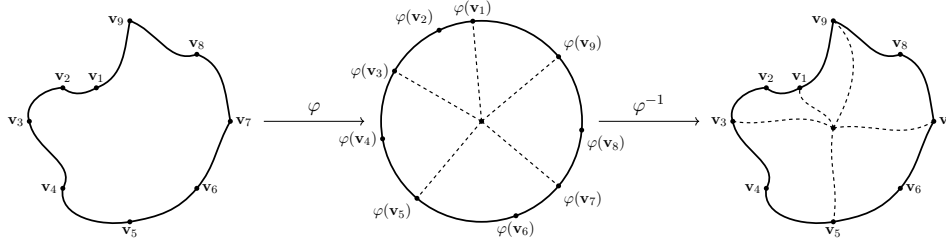


FIG. 1.  $\mathcal{Y}$  is homeomorphic to an open disk in the case of  $n_- = 0$ . The dashed straight lines represent the division of the disk, and the dashed curves represent the division of  $\mathcal{Y}$ .

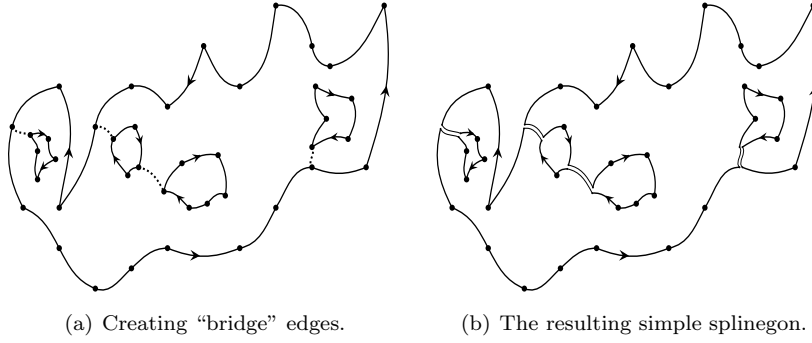


FIG. 2. Transforming a splinegon with holes into a simple splinegon.

A Yin set  $\mathcal{Y} \in \mathbb{Y}_c$  is called a *simple splinegon* if it is homeomorphic to an open disk, i.e., if it is categorized as the second case  $\mathcal{J}^+$  in (2.5) with  $n_- = 0$ . A *splinegon with holes* is a Yin set in  $\mathbb{Y}_c$  categorized as the second case  $\mathcal{J}^+$  with  $n_- > 0$ .

**THEOREM 2.5.** *Each bounded Yin set  $\mathcal{Y} \subset \mathbb{R}^2$  can be partitioned into a regularized union of a finite number of curved quadrilaterals and triangles.*

*Proof.* It suffices to prove the statement for bounded and connected Yin sets in  $\mathbb{Y}_c$ . The boundedness of  $\mathcal{Y}$  precludes the first case  $\mathcal{J}^-$  in (2.5) and Theorem 2.4 dictates that  $\mathcal{Y}$  be represented as  $\mathcal{J}^+$ . By (2.5), we only need to consider two possibilities.

- $n_- = 0$ :  $\mathcal{Y}$  is a simple splinegon homeomorphic to an open disk. If  $\mathcal{Y}$  has no more than four vertices, the conclusion holds trivially since it is already a curved quadrilateral or triangle. Otherwise we map  $\mathcal{Y}$  by a homeomorphism  $\varphi$  to an open disk, partition the disk by connecting its center to every other vertex on the circle, and the images of these radii under  $\varphi^{-1}$  partition  $\mathcal{Y}$  into a regularized union of curved quadrilaterals and triangles. By Definition 2.2,  $\mathcal{Y}$  is semianalytic and thus the number of quadrilaterals is finite. As shown in Figure 1, the number of triangles is at most one: the triangle exists if and only if the number of vertices of  $\mathcal{Y}$  is odd.
- $n_- > 0$ :  $\mathcal{Y}$  is a splinegon with holes. As shown in Figure 2, we add a pair of “bridge” edges from a vertex of each  $\gamma_j^-$  to some vertex in  $\gamma^+$  of  $\mathcal{J}^+$  in (2.5); the existence of these bridge edges is guaranteed by the connectedness of  $\mathcal{Y}$ . Now that  $\mathcal{Y}$  is approximated arbitrarily well by a simple splinegon, the rest of the proof follows from the previous paragraph.  $\square$

**3. Algorithm.** We embed the problem domain  $\Omega$  inside a rectangular region  $\Omega_R \in \mathbb{Y}_c$  and divide  $\Omega_R$  by structured rectangular grids into control volumes or cells,

$$(3.1) \quad \mathbf{C}_i := (i\mathbf{h}, (\mathbf{i} + \mathbb{1})h),$$

where  $h$  is the uniform grid size,  $\mathbf{i} \in \mathbb{Z}^2$  a multi-index, and  $\mathbb{1} \in \mathbb{Z}^2$  the multi-index with all components equal to one. The assumption of  $h$  being uniform is for ease of exposition only, as our algorithm also applies to non-uniform grids. In both cases, we have  $\Omega_R = \cup_{\mathbf{i}}^{\perp\perp} \mathbf{C}_i$  where  $\cup^{\perp\perp}$  is the regularized union operation in [Theorem 2.3](#).

For an irregular domain  $\Omega$ , we define the  $i$ th cut cell and the  $i$ th cut boundary as

$$(3.2) \quad \mathcal{C}_i := \mathbf{C}_i \cap \Omega; \quad \mathcal{S}_i := \mathbf{C}_i \cap \partial\Omega,$$

where  $\cap$  is the intersection operation in [Theorem 2.3](#). Clearly we have  $\Omega = \cup_{\mathbf{i}}^{\perp\perp} \mathcal{C}_i$ .

A cut cell is classified as an *empty cell*, a *pure cell*, or an *interface cell* if it satisfies  $\mathcal{C}_i = \emptyset$ ,  $\mathcal{C}_i = \mathbf{C}_i$ , or otherwise, respectively.

The averaged values of a scalar function  $g : \Omega \rightarrow \mathbb{R}$  over a nonempty cut cell  $\mathcal{C}_i$  and a cut boundary  $\mathcal{S}_i$  are respectively,

$$(3.3) \quad \langle g \rangle_i := \frac{1}{\|\mathcal{C}_i\|} \iint_{\mathcal{C}_i} g(\mathbf{x}) \, d\mathbf{x}; \quad \langle\langle g \rangle\rangle_i := \frac{1}{\|\mathcal{S}_i\|} \int_{\mathcal{S}_i} g(\mathbf{x}) \, d\mathbf{x},$$

where  $\|\mathcal{C}_i\|$  is the volume of  $\mathcal{C}_i$  and  $\|\mathcal{S}_i\|$  the length of  $\mathcal{S}_i$ .

The time interval  $[0, T]$  is partitioned into  $N_T$  subintervals with a uniform time step size  $k = \frac{T}{N_T}$  so that  $t_n := nk$  for  $n = 0, \dots, N_T$ . To numerically solve the advection equation [\(1.1\)](#), it suffices to approximate  $\langle \rho(\mathbf{x}, t_{n+1}) \rangle_i$  for an arbitrary cut cell  $\mathcal{C}_i$  from the given velocity field  $\mathbf{u}$ , the initial condition  $\langle \rho \rangle_i^n \approx \langle \rho(\mathbf{x}, t_n) \rangle_i$ , and the boundary condition of  $\rho$ .

**DEFINITION 3.1 (SLFV).** *The SLFV method is a finite volume method for solving the advection equation [\(1.1\)](#) by approximating  $\langle \rho(\mathbf{x}, t_{n+1}) \rangle_i$  with steps as follows.*  
*(SLFV-1) For each cut cell  $\mathcal{C}_i \subset \Omega$  and any scalar function  $g : \mathcal{C}_i \rightarrow \mathbb{R}$ , determine a quadrature formula*

$$(3.4) \quad I_i(g) := \sum_{m=1}^M \omega_{i,m} g(\mathbf{x}_{i,m})$$

*by calculating the nodes  $\{\mathbf{x}_{i,m}\}_{m=1}^M$  and the weights  $\{\omega_{i,m}\}_{m=1}^M$  of  $I_i$  from [\(3.11\)](#) in [Subsection 3.1](#) and the partitioning of  $\mathcal{C}_i$  in [Theorem 2.5](#).*

*(SLFV-2) For each node  $\mathbf{x}_{i,m}$ , compute a set of points  $\{\mathbf{x}_{i,m}^{n+c_i} \approx \phi_{t_{n+1}}^{-(1-c_i)k}(\mathbf{x}_{i,m})\}$  on the pathline  $\Phi_{t_{n+1}}^{-k}(\mathbf{x}_{i,m})$  by solving the ODE [\(2.1\)](#). The approximate preimage of  $\mathbf{x}_{i,m}$  at  $t_n$  is denoted by  $\overleftarrow{\mathbf{x}}_{i,m} := \mathbf{x}_{i,m}^{n+0}$ ; see [Figure 3\(a\)](#).*

*(SLFV-3) If  $\overleftarrow{\mathbf{x}}_{i,m} \notin \Omega$ , calculate  $\tilde{\rho}^{n+1}(\mathbf{x}_{i,m}) \approx \rho(\mathbf{x}_{i,m}, t_{n+1})$  by [\(3.12\)](#) in [Subsection 3.2](#).*

*(SLFV-4) Otherwise approximate  $\rho(\overleftarrow{\mathbf{x}}_{i,m}, t_n)$  by  $f(\overleftarrow{\mathbf{x}}_{i,m})$ , the value of a local bi-variate polynomial  $f$  fitted from the initial condition  $\langle \rho \rangle_i^n$  and the boundary condition of  $\rho$  at  $t_n$ ; see [Subsection 3.3](#) for an elaboration of this process. Then calculate  $\tilde{\rho}^{n+1}(\mathbf{x}_{i,m}) \approx \rho(\mathbf{x}_{i,m}, t_{n+1})$  by solving [\(1.3\)](#) with an  $s$ -stage Runge-Kutta (RK) method,*

$$(3.5) \quad \begin{aligned} \forall i = 1, \dots, s, \quad Y_i &= S(\mathbf{x}_{i,m}^{n+c_i}, t_n + c_i k), \\ \tilde{\rho}^{n+1}(\mathbf{x}_{i,m}) &= f(\overleftarrow{\mathbf{x}}_{i,m}) + k \sum_{j=1}^s b_j Y_j, \end{aligned}$$

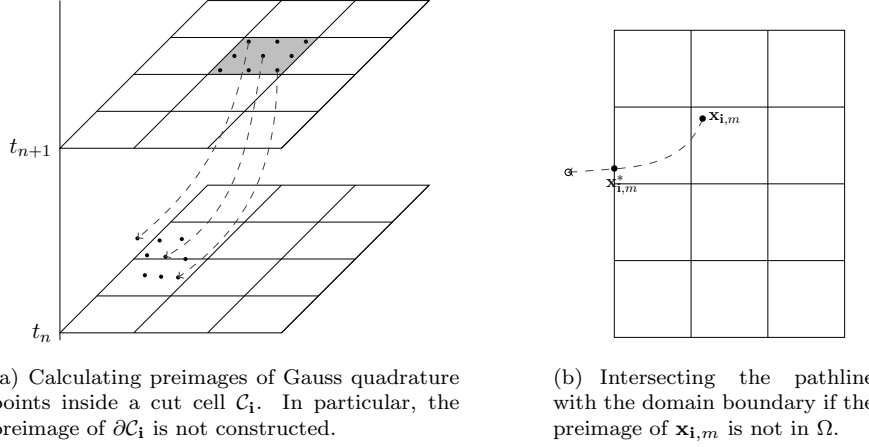


FIG. 3. The backtracking of Gauss quadrature points inside a control volume. The gray quadrilateral represents the cut cell  $C_i$  for which the averaged value of  $p$  at time  $t_{n+1}$  is sought. A dashed line with an arrowhead represents a pathline obtained by numerically solving the ODE (2.1). (a) The solid dots at  $t_{n+1}$  represent the Gauss quadrature points while those at  $t_n$  denote their preimages. If the preimage of a quadrature point  $\mathbf{x}_{i,m}$  is not in  $\Omega$ , the pathline of  $\mathbf{x}_{i,m}$  must intersect the domain boundary at some time  $t^* \in (t_n, t_{n+1})$ . (b)  $\mathbf{x}_{i,m}$  and  $\mathbf{x}_{i,m}^*$  represent the Gauss quadrature point at time  $t_{n+1}$  and the intersection of its pathline with the domain boundary at  $t^*$ , respectively. The hollow circle denotes the preimage of  $\mathbf{x}_{i,m}$ .

where  $b_j$ ,  $c_i$  are coefficients of the RK method and  $\mathbf{x}_{i,m}^{n+c_i}$ 's points of the pathline  $\Phi_{t_{n+1}}^{-k}(\mathbf{x}_{i,m})$  obtained in (SLFV-2).  
 (SLFV-5) Repeat (SLFV-2,3,4) for each quadrature node  $\mathbf{x}_{i,m}$  in (3.4) and set the solution of SLFV for the cut cell  $C_i$  as  $\langle \rho \rangle_i^{n+1} := I_i(\tilde{\rho}^{n+1}) \approx \langle \rho(\mathbf{x}, t_{n+1}) \rangle_i$ .

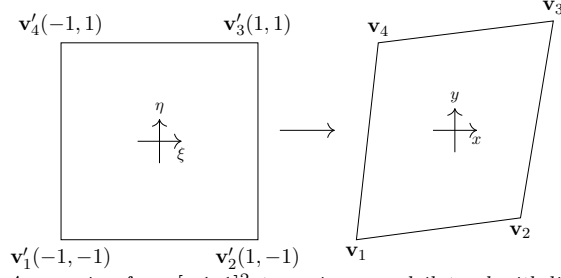
The above steps of the SLFV method are orthogonal in that the subproblems of complex geometry, temporal integration, and polynomial reconstruction are decoupled. Consequently, fourth- and higher-order accuracy both in time and in space can be achieved in a flexible manner. In addition, the steps of SLFV remain the same regardless of the source term  $S$  being zero or not; this answers (Q-3).

*Remark 3.2.* In a family of conservative semi-Lagrangian methods [19, 10, 14], the preimage of the boundary of a control volume is constructed and its intersection with nearby control volumes is computed. In our SLFV method, however, this intersection is avoided by calculating the preimages of Gauss quadrature points; see Figure 3(a). Only for handling incoming penetration domains would we compute the intersection of a particle pathline and the domain boundary; see Figure 3(b).

In the rest of this section, we fully explain the key components of SLFV.

**3.1. Gauss quadrature on interface cells.** Since  $\partial\Omega$  is of co-dimension one, most nonempty cut cells are pure cells, for which Gauss quadrature formulas can be obtained by tensor products of one-dimensional formulas and will not be discussed further. Here we design a three-step quadrature formula for interface cells.

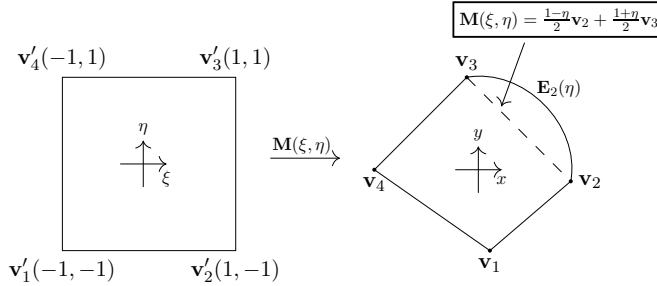
- (GQI-1) Partition the interface cell  $C_i$  into a union of curved quadrilaterals and triangles; see Theorem 2.5 and Figure 1 for such an algorithm.
- (GQI-2) Calculate integrals on each curved quadrilateral or triangle via an isoparametric mapping and the blending function method [35, p.99].
- (GQI-3) Sum up the subintegrals to approximate the integral over  $C_i$ .

FIG. 4. A mapping from  $[-1, 1]^2$  to a given quadrilateral with linear edges.

The first part of (GQI-2) is an isoparametric mapping  $\mathbf{M}(\xi, \eta) = \sum_{i=1}^4 N_i(\xi, \eta) \mathbf{v}_i$  where  $\mathbf{v}_i$ 's are vertices of a quadrilateral and the Lagrangian shape functions are

$$\begin{aligned} N_1(\xi, \eta) &= \frac{1}{4}(1 - \xi)(1 - \eta), & N_2(\xi, \eta) &= \frac{1}{4}(1 + \xi)(1 - \eta), \\ N_3(\xi, \eta) &= \frac{1}{4}(1 + \xi)(1 + \eta), & N_4(\xi, \eta) &= \frac{1}{4}(1 - \xi)(1 + \eta). \end{aligned}$$

As shown in Figure 4,  $\mathbf{M}$  maps  $[-1, 1]^2$  to the given quadrilateral. Hereafter we denote by  $\mathbf{E}_i := (E_{i,x}, E_{i,y})$  the parametrization of the  $i$ th (linear or curved) edge  $\widehat{\mathbf{v}_i \mathbf{v}_{i+1}}$  of a quadrilateral with the convention  $\mathbf{v}_5 = \mathbf{v}_1$ .

FIG. 5. A mapping from  $[-1, 1]^2$  to a quadrilateral with one curved edge.

Next, we illustrate the main idea of the blending function method by the simple case in the right-hand side (RHS) of Figure 5, where only one edge of the quadrilateral is curved. The canonical square  $[-1, 1]^2$  is mapped to the curved quadrilateral by

$$\begin{aligned} \mathbf{M}(\xi, \eta) &= \frac{1}{4}(1 - \xi)(1 - \eta) \mathbf{v}_1 + \frac{1}{4}(1 + \xi)(1 - \eta) \mathbf{v}_2 + \frac{1}{4}(1 + \xi)(1 + \eta) \mathbf{v}_3 \\ (3.6) \quad &+ \frac{1}{4}(1 - \xi)(1 + \eta) \mathbf{v}_4 + \left( \mathbf{E}_2(\eta) - \frac{1 - \eta}{2} \mathbf{v}_2 - \frac{1 + \eta}{2} \mathbf{v}_3 \right) \frac{1 + \xi}{2}, \end{aligned}$$

where the first four terms represent the linear isoparametric mapping and the last a product of two functions: the one in the parentheses represents the difference between  $\mathbf{E}_2(\eta)$  and the chord joining  $\mathbf{v}_2$  and  $\mathbf{v}_3$  while the other is a linear function that equals 1 on  $\widehat{\mathbf{v}_2 \mathbf{v}_3}$  and 0 on  $\widehat{\mathbf{v}_4 \mathbf{v}_1}$ . The mapping in (3.6) simplifies to

$$(3.7) \quad \mathbf{M}(\xi, \eta) = \frac{1}{4}(1 - \xi)(1 - \eta) \mathbf{v}_1 + \frac{1}{4}(1 - \xi)(1 + \eta) \mathbf{v}_4 + \mathbf{E}_2(\eta) \frac{1 + \xi}{2}.$$

The above mapping generalizes in a straightforward manner to the general case



where all edges of the quadrilateral are curved:

$$(3.8) \quad \mathbf{M}(\xi, \eta) = \frac{1}{2} [(1 - \eta)\mathbf{E}_1(\xi) + (1 + \xi)\mathbf{E}_2(\eta) + (1 + \eta)\mathbf{E}_3(\xi) + (1 - \xi)\mathbf{E}_4(\eta)] - \sum_{i=1}^4 N_i(\xi, \eta) \mathbf{v}_i.$$

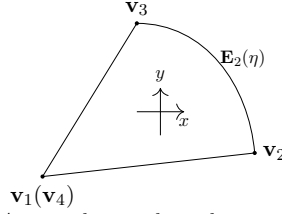


FIG. 6. A curved triangle with one curved edge.

A curved triangle is treated as a special quadrilateral with one edge collapsed into a single vertex. In the case of Figure 6, the mapping in (3.7) reduces to

$$(3.9) \quad \mathbf{M}(\xi, \eta) = \frac{1 - \xi}{2} \mathbf{v}_1 + \frac{1 + \xi}{2} \mathbf{E}_2(\eta),$$

whose Jacobian matrix is

$$J = \begin{pmatrix} -\frac{1}{2}x_1 + \frac{1}{2}E_{2,x}(\eta) & \frac{1+\xi}{2}E'_{2,x}(\eta) \\ -\frac{1}{2}y_1 + \frac{1}{2}E_{2,y}(\eta) & \frac{1+\xi}{2}E'_{2,y}(\eta) \end{pmatrix}.$$

As  $\xi$  approaches  $-1$ , the determinant  $|J|$  of the Jacobian matrix approaches zero, indicating a singularity at  $\mathbf{v}_1$ . Fortunately, it is well known that all nodes of a Gauss formula are contained in the integral domain and hence, for any fixed degree of exactness, their distances to the integral boundary are bounded below by a positive real number. Thus  $|J|$  also has a positive lower bound that never approaches zero and the mapping in (3.9) remains valid for sending the quadrature nodes in  $[-1, 1]^2$  to those inside the triangle.

For a triangle whose edges are all curved, the mapping in (3.8) reduces to

$$(3.10) \quad \mathbf{M}(\xi, \eta) = \frac{1}{2} ((1 - \eta)\mathbf{E}_1(\xi) + (1 + \xi)\mathbf{E}_2(\eta) + (1 + \eta)\mathbf{E}_3(\xi)) - N_2(\xi, \eta)\mathbf{v}_2 - N_3(\xi, \eta)\mathbf{v}_3.$$

To sum up, the Gauss formula of approximating the integral of a scalar function  $g$  over a curved quadrilateral or a curved triangle is summarized as

$$(3.11) \quad I(g) := \sum_{i'=1}^{m_\xi} \sum_{j'=1}^{m_\eta} \omega_{i',j'} g(\mathbf{M}(\xi_{i'}, \eta_{j'})),$$

where  $\mathbf{M}$  is given by (3.8) and (3.10) for a curved quadrilateral and a curved triangle, respectively,  $\{\xi_{i'}\}_{i'=1}^{m_\xi}$ ,  $\{\eta_{j'}\}_{j'=1}^{m_\eta}$  and  $\{\omega_{i'}\}_{i'=1}^{m_\xi}$ ,  $\{\omega_{j'}\}_{j'=1}^{m_\eta}$  are the nodes and weights of the one-dimensional Gauss formula in the  $\xi$  and  $\eta$  directions, respectively, and  $\omega_{i',j'} := \omega_{i'}\omega_{j'}|J(\xi_{i'}, \eta_{j'})|$ .

Our Gauss formula (GQI-1,2,3) answers (Q-1) since it applies to irregular domains with arbitrarily complex topology and geometry.

**3.2. Handling incoming penetration domains.** Recall from (1.2) that a/an (incoming) penetration domain is a non-periodic domain that satisfies  $\Gamma^- \neq \emptyset$ . In this case the pathline  $\Phi_{t_{n+1}}^{-k}(\mathbf{x}_{i,m})$  constructed in (SLFV-2) might intersect  $\partial\Omega$ . The existence of such an intersection is implied by the condition  $\overleftarrow{\mathbf{x}_{i,m}} \notin \Omega$  in (SLFV-3), which can be detected by shooting a ray from  $\overleftarrow{\mathbf{x}_{i,m}}$  and verifying that the number of intersections of the ray to  $\partial\Omega$  is even.

Suppose the pathline  $\Phi_{t_{n+1}}^{-k}(\mathbf{x}_{i,m})$  intersects  $\partial\Omega$  at  $\mathbf{x}_{i,m}^*$  and  $t^* \in (t_n, t_{n+1})$ , as shown in Figure 3(b), we can approximate  $\rho(\mathbf{x}_{i,m}, t_{n+1})$  from the boundary condition  $\rho_{bc}(\mathbf{x}_{i,m}^*, t^*)$  by solving (1.3) along a shortened pathline  $\Phi_{t^*}^{t_{n+1}-t^*}(\mathbf{x}_{i,m}^*)$  with  $\rho_{bc}(\mathbf{x}_{i,m}^*, t^*)$  as its initial condition.

To determine  $\mathbf{x}_{i,m}^*$  and  $t^*$ , we define a function  $\mathbf{F}(s, t) := \gamma(s) - \phi_{t_{n+1}}^{t-t_{n+1}}(\mathbf{x}_{i,m})$  where  $s \in [0, L]$  and  $\gamma := (\gamma_x, \gamma_y)$  is a local arc of  $\partial\Omega$  that covers  $\mathbf{x}_{i,m}^*$ . Then we solve the nonlinear equation  $\mathbf{F}(s^*, t^*) = (0, 0)$  with the Newton iteration,

$$\begin{pmatrix} s^{(\iota+1)} \\ t^{(\iota+1)} \end{pmatrix} = \begin{pmatrix} s^{(\iota)} \\ t^{(\iota)} \end{pmatrix} - \left( \frac{\partial \mathbf{F}}{\partial (s, t)} \begin{pmatrix} s^{(\iota)} \\ t^{(\iota)} \end{pmatrix} \right)^{-1} \mathbf{F} \begin{pmatrix} s^{(\iota)} \\ t^{(\iota)} \end{pmatrix}^\top,$$

where the Jacobian matrix, by the flow map  $\phi$  in (2.2), is

$$\frac{\partial \mathbf{F}}{\partial (s, t)}(s, t) = \begin{pmatrix} \gamma'_x(s) & -u \left( \phi_{t_{n+1}}^{t-t_{n+1}}(\mathbf{x}_{i,m}), t \right) \\ \gamma'_y(s) & -v \left( \phi_{t_{n+1}}^{t-t_{n+1}}(\mathbf{x}_{i,m}), t \right) \end{pmatrix},$$

and  $\mathbf{u} = (u, v)^\top$ .

The iteration starts with  $t^{(0)} = t_{n+1}$  and  $\gamma(s^{(0)})$ , the point in  $\partial\Omega$  closest to  $\mathbf{x}_{i,m}$ , and continues until  $\|\mathbf{F}(s^{(\iota)}, t^{(\iota)})\|_2$  falls below a user-defined threshold or the maximum number of iterations is reached.

After determining  $t^*$  and  $\mathbf{x}_{i,m}^*$ , we set  $k^* := t_{n+1} - t^*$  and solve a modified version of (3.5) with  $t^*$  as the initial time and  $\rho_{bc}(\mathbf{x}_{i,m}^*, t^*)$  as the initial value,

$$(3.12) \quad \begin{aligned} \forall i = 1, \dots, s, \quad Y_i &= S(\mathbf{x}_{i,m}(t^* + c_i k^*), t^* + c_i k^*), \\ \tilde{\rho}^{n+1}(\mathbf{x}_{i,m}) &= \rho_{bc}(\mathbf{x}_{i,m}^*, t^*) + k^* \sum_{j=1}^s b_j Y_j. \end{aligned}$$

The above steps constitute an efficient and accurate treatment of incoming penetration conditions, answering (Q-2).

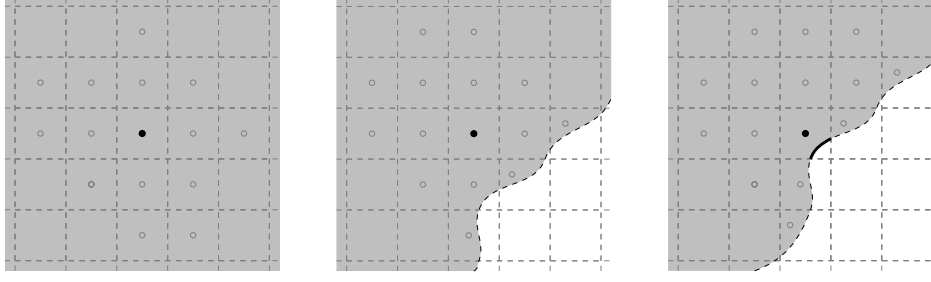
**3.3. Polynomial reconstruction from cell averages.** We start with polynomial fitting of cell averages.

**DEFINITION 3.3.** Denote by  $\Pi_q$  the linear space of all real-coefficient bi-variate polynomials of degree no greater than  $q$  and write  $N := \dim \Pi_q$ . For a finite class of pairwise disjoint Yin sets  $\mathcal{T} := \{C_{i_1}, \dots, C_{i_N}\}$  and a corresponding set of values  $f_1, \dots, f_N \in \mathbb{R}$ , the Lagrange interpolation problem (LIP) for cell averages seeks a polynomial  $f \in \Pi_q$  such that  $\langle f \rangle_{i_j}$ , the average of  $f$  over  $C_{i_j}$ , equals  $f_j$  for each  $j$ , i.e.,

$$(3.13) \quad \forall j = 1, \dots, N, \quad \langle f \rangle_{i_j} = f_j.$$

A LIP is said to be *unisolvent* if for *any* given sequence of cell averages  $(f_j)_{j=1}^N$  there exists  $f \in \Pi_q$  satisfying (3.13); then we also call the set  $\mathcal{T}$  a *poised lattice*.

For a pure cell far from the domain boundary, we use the standard poised lattice shown in Figure 7(a). Whenever the stencil in Figure 7(a) involves an empty cell,



(a) The standard stencil for pure cells far from the domain boundary. (b) A lattice for a pure cell near the domain boundary. (c) A lattice for an interface cell near the domain boundary.

FIG. 7. Poised lattices for the fifth-order polynomial reconstruction from cell averages. The gray region represents the computational domain. The solid dot marks the target cut cell  $C_i$ , while solid and hollow dots together represent the poised lattice. The solid curve represents the additional boundary portion within the target cell. The three subplots cover all cases.

we employ the AI-aided algorithm in [42] to generate a poised lattice. Figure 7(b) and Figure 7(c) demonstrate poised lattices generated by this AI-aided algorithm for a pure cell near the domain boundary and an interface cell, respectively. With an optimal complexity, this AI-aided algorithm obviates the need for ghost cells at an irregular boundary; see [42, Fig. 3] for more details. As shown in Figure 7(c), the cut boundary  $\mathcal{S}_i$  of an interface cell  $C_i$  is also added into the generated lattice to incorporate the boundary condition. Then we define

$$\boldsymbol{\rho} := [\rho_1, \dots, \rho_N, \rho_b]^\top = [\langle \rho \rangle_{\mathbf{i}_1}, \dots, \langle \rho \rangle_{\mathbf{i}_N}, \langle \langle \rho \rangle \rangle_{\mathbf{i}}]^\top \in \mathbb{R}^{N+1}.$$

Denote by  $\boldsymbol{\alpha} := [\alpha_1, \dots, \alpha_N]^\top$  coefficients of a polynomial  $f(\mathbf{x}) = \sum_{i=1}^N \alpha_i \psi_i(\mathbf{x}) \in \Pi_q$ , where  $\psi_i$ 's are the monomial bases of  $\Pi_q$ . To obtain a  $(q+1)$ th-order approximation of  $\rho(\mathbf{x}, t_n)$ , we determine  $\boldsymbol{\alpha}$  by minimizing

$$\begin{aligned} & \sum_{j=1}^N w_j \left| \langle f \rangle_{\mathbf{i}_j} - \rho_j \right|^2 + w_b \left| \langle \langle f \rangle \rangle_{\mathbf{i}} - \rho_b \right|^2 \\ &= \sum_{j=1}^N w_j \left( \sum_{i=1}^N \alpha_i \langle \psi_i \rangle_{\mathbf{i}_j} - \rho_j \right)^2 + w_b \left( \sum_{i=1}^N \alpha_i \langle \langle \psi_i \rangle \rangle_{\mathbf{i}} - \rho_b \right)^2 \\ &= (\boldsymbol{\alpha}^\top M - \boldsymbol{\rho}^\top) W (M^\top \boldsymbol{\alpha} - \boldsymbol{\rho}) = \|M^\top \boldsymbol{\alpha} - \boldsymbol{\rho}\|_W^2, \end{aligned}$$

where  $W$  is a positive definite diagonal matrix with  $W := \text{diag}(w_1, \dots, w_N, w_b)$ , the energy norm is given by  $\|\mathbf{v}\|_W := \sqrt{\mathbf{v}^\top W \mathbf{v}}$ , and

$$(3.14) \quad M = \begin{pmatrix} \langle \psi_1 \rangle_{\mathbf{i}_1} & \cdots & \langle \psi_1 \rangle_{\mathbf{i}_N} & \langle \langle \psi_1 \rangle \rangle_{\mathbf{i}} \\ \vdots & \ddots & \vdots & \vdots \\ \langle \psi_N \rangle_{\mathbf{i}_1} & \cdots & \langle \psi_N \rangle_{\mathbf{i}_N} & \langle \langle \psi_N \rangle \rangle_{\mathbf{i}} \end{pmatrix} \in \mathbb{R}^{N \times (N+1)}.$$

In this work, we set  $w_j := \min\{\|\mathbf{i}_j - \mathbf{i}\|_2^{-1}, w_{\max}\}$ ,  $w_b := w_{\max}$ , and  $w_{\max} = 2$  to avoid large weights.

For interface cells, the above minimization leads to a problem of weighted least squares, which we solve by QR factorization. For pure cells, the last column of  $M$  in

(3.14) is omitted, and the square linear system  $M^\top \alpha = \rho$  is solved directly for the polynomial coefficients. In both cases, we obtain a polynomial  $f(\mathbf{x}) = \sum_{i=1}^N \alpha_i \psi_i(\mathbf{x})$  by which we can evaluate point values of  $\rho$  at the preimages of nodes of Gauss formulas.

Finally, we give some details on the stability of our polynomial reconstruction.

- (a) The total degree of the bi-variate polynomial is limited to 8 to prevent wild oscillations of polynomial interpolation on uniform grid (the Runge phenomenon).
- (b) To avoid small volume fractions, any cut cell that satisfies  $\|\mathcal{C}_i\| < \epsilon h^2$  is merged into one of its adjacent cells so that the merged cell has a volume fraction no less than  $\epsilon$ . Similarly, any interface cell with  $\|\mathcal{S}_i\| < \epsilon h$  is merged into an adjacent cut cell so that the cut boundary has a length ratio no less than  $\epsilon$ . In this work, we set the user-specified merging threshold to  $\epsilon = 0.1$ , which constraints the variation of volume fractions to one order of magnitude and guarantees good conditioning of the linear system for polynomial coefficients.
- (c) The AI-aided algorithm for poised lattice generation is originally developed for *finite difference* formulations and also works well for *finite volume* discretizations, so long as each cell only contributes *one* equation to the linear system. If we insist on  $N$  equations with an interface cell contributing two equations, one from the cell average and the other from the face average over the cut boundary, there might exist pathological cases that lead to ill-conditioning or even singularity of the corresponding linear system. It is also difficult to solve this problem analytically. Fortunately, a simple solution to this problem is to treat the equation from the cut boundary as one extra condition so that the over-determined linear system with  $N + 1$  equations contains a poised lattice of  $N$  cells with good conditioning. Then QR factorization gives a well-conditioned solution of the least square problem.
- (d) Apart from (c), additional points are sometimes appended into a poised lattice so that the condition number of the corresponding linear system is further lowered to a local minimum. In this type of least squares, the condition number is well under control via the number of additional points; see [42, Fig. 8] for a few illustrations.

**4. Analysis.** In this section, we prove the convergence rates of the SLFV method. We start by examining Gauss formulas on curved quadrilaterals and triangles.

**LEMMA 4.1.** *Denote by  $\mathbf{E}_i := (E_{i,x}, E_{i,y})$  the  $i$ th edge of a curved quadrilateral or triangle  $\mathcal{Q} \subset \mathbb{R}^2$ . Suppose that  $E_{i,x}$  and  $E_{i,y}$  are both polynomials  $[-1, 1] \mapsto \mathbb{R}$  of degree at most  $q$ . Then the quadrature formula in (3.11) is exact for any bi-variate polynomial  $g : \mathcal{Q} \rightarrow \mathbb{R}$  of degree at most  $\kappa$  in each variable provided that  $\min(m_\xi, m_\eta) \geq \lceil \frac{(\kappa+2)q}{2} \rceil$  holds for  $m_\xi$  and  $m_\eta$  in (3.11).*

*Proof.* The variable substitution of  $(x, y) = \mathbf{M}(\xi, \eta)$  in (3.11) yields

$$\iint_{\mathcal{Q}} g(x, y) \, dx dy = \int_{-1}^1 \int_{-1}^1 g(\mathbf{M}(\xi, \eta)) |J(\xi, \eta)| \, d\xi d\eta,$$

where  $J(\xi, \eta)$  is the Jacobian matrix of  $\mathbf{M}(\xi, \eta)$ . Since  $E_{i,x}(l)$  and  $E_{i,y}(l)$  are both polynomials of degree at most  $q$ , (3.8) and (3.10) imply that  $\mathbf{M}(\xi, \eta)$  is a polynomial of degree at most  $q$  in each variable. Hence the composite function  $g(\mathbf{M}(\xi, \eta))$  is a polynomial of degree at most  $\kappa q$  in each variable and the determinant of the Jacobian matrix,  $|J(\xi, \eta)|$ , is a polynomial of degree at most  $2q - 1$  in each variable. Thus the product  $g(\mathbf{M}(\xi, \eta)) |J(\xi, \eta)|$  is a polynomial of degree at most  $(\kappa + 2)q - 1$  in each variable. Therefore, for a one-dimensional Gauss formula to be exact, it suffices to have  $\min(m_\xi, m_\eta) \geq \lceil \frac{(\kappa+2)q}{2} \rceil$ .  $\square$

[Lemma 4.1](#) is a key in analyzing the accuracy of the SLFV method. We also need

LEMMA 4.2. *Consider the initial value problem (IVP)*

$$\mathbf{w}'(t) = \mathbf{f}(\mathbf{w}(t), t), \quad \mathbf{w}(0) = \mathbf{w}_0,$$

where  $\mathbf{f}(\mathbf{w}, t)$  is Lipschitz continuous in  $\mathbf{w}$  and continuous in  $t \in [0, T]$ . Let  $\mathbf{v}(t)$  be the solution of the perturbed IVP over  $[0, T]$ ,

$$\mathbf{v}'(t) = \mathbf{f}(\mathbf{v}(t), t) + \boldsymbol{\delta}(t), \quad \mathbf{v}(0) = \mathbf{v}_0 := \mathbf{w}_0 + \boldsymbol{\varepsilon}_0.$$

Suppose there exists a constant  $\varepsilon > 0$  such that  $\|\boldsymbol{\varepsilon}_0\| < \varepsilon$  and  $\|\boldsymbol{\delta}(t)\| < \varepsilon$ , then

$$\forall t \in [0, T], \quad \|\mathbf{v}(t) - \mathbf{w}(t)\| \leq (1 + Ct)\varepsilon,$$

where  $C := 1 + L \exp(LT)(1 + T)$  and  $L$  is the Lipschitz constant of the RHS  $\mathbf{f}$ .

*Proof.* Since  $\mathbf{v}(t) - \mathbf{w}(t) = \mathbf{v}_0 - \mathbf{w}_0 + \int_0^t [\mathbf{f}(\mathbf{v}(\tau), \tau) - \mathbf{f}(\mathbf{w}(\tau), \tau) + \boldsymbol{\delta}(\tau)] d\tau$ , we have, from the triangular inequality and the Lipschitz condition,

$$(4.1) \quad \|\mathbf{v}(t) - \mathbf{w}(t)\| \leq (1 + t)\varepsilon + \int_0^t L \|\mathbf{v}(\tau) - \mathbf{w}(\tau)\| d\tau.$$

To estimate the integral, we define a function  $g : [0, T] \rightarrow \mathbb{R}$ ,

$$g(\tau) := \exp(-L\tau) \int_0^\tau L \|\mathbf{v}(r) - \mathbf{w}(r)\| dr,$$

so that  $g'(\tau) = L \exp(-L\tau) (\|\mathbf{v}(\tau) - \mathbf{w}(\tau)\| - \int_0^\tau L \|\mathbf{v}(r) - \mathbf{w}(r)\| dr)$ . Since  $g(0) = 0$ , we have  $g(t) = g(t) - g(0) = \int_0^t g'(\tau) d\tau$ . It follows that

$$\begin{aligned} g(t) &= \exp(-Lt) \int_0^t L \|\mathbf{v}(r) - \mathbf{w}(r)\| dr \\ &= \int_0^t L \exp(-L\tau) \left( \|\mathbf{v}(\tau) - \mathbf{w}(\tau)\| - \int_0^\tau L \|\mathbf{v}(r) - \mathbf{w}(r)\| dr \right) d\tau \\ &\leq \int_0^t L \exp(-L\tau)(1 + \tau)\varepsilon d\tau, \end{aligned}$$

where the inequality follows from [\(4.1\)](#). Multiply  $\exp(Lt)$  to the first and third lines and we have  $\int_0^t L \|\mathbf{v}(\tau) - \mathbf{w}(\tau)\| d\tau \leq \int_0^t L \exp(L(t - \tau))(1 + \tau)\varepsilon d\tau$ , which, together with [\(4.1\)](#) and the integral mean value theorem, yields

$$\|\mathbf{v}(t) - \mathbf{w}(t)\| \leq (1 + t)\varepsilon + \int_0^t L \exp(L(t - \tau))(1 + \tau)\varepsilon d\tau \leq (1 + Ct)\varepsilon. \quad \square$$

THEOREM 4.3. *Suppose the solution of [\(1.1\)](#) is sufficiently smooth and the domain  $\Omega \in \mathbb{Y}$  is approximated by a Yin set  $\Omega_c \in \mathbb{Y}_c$ , whose boundary curves consist of cubic splines of which the maximal chordal length of adjacent breakpoints is denoted by  $h_L$ . Then, in the max-norm, the SLFV method in [Definition 3.1](#) with  $k = O(h)$  is*

- *fourth-order convergent both in time and in space if we choose  $h_L = O(h)$ , a 4th-order RK method in [\(3.5\)](#), [\(3.12\)](#), and (SLFV-2), a 5th-order polynomial reconstruction in (SLFV-4), and Gauss formulas in [\(3.11\)](#) with  $m_\xi, m_\eta \geq 3$  for pure cells and  $m_\xi, m_\eta \geq 9$  for interface cells.*

- *sixth-order convergent both in time and in space if we choose  $h_L = O(h^{\frac{3}{2}})$ , a 6th-order RK method in (3.5), (3.12), and (SLFV-2), a 7th-order polynomial reconstruction in (SLFV-4), and Gauss formulas in (3.11) with  $m_\xi, m_\eta \geq 4$  for pure cells and  $m_\xi, m_\eta \geq 12$  for interface cells.*
- *eighth-order convergent both in time and in space if we choose  $h_L = O(h^2)$ , an 8th-order RK method in (3.5), (3.12), and (SLFV-2), a 9th-order polynomial reconstruction in (SLFV-4), and Gauss formulas in (3.11) with  $m_\xi, m_\eta \geq 5$  for pure cells and  $m_\xi, m_\eta \geq 15$  for interface cells.*

*Proof.* The approximation of  $\Omega$  with  $\Omega_c$  is fourth-, sixth-, and eighth-order accurate when  $h_L = O(h)$ ,  $O(h^{\frac{3}{2}})$ , and  $O(h^2)$ , respectively [15]. Here we only give the proof for the fourth-order case, as those for other cases are similar.

Define a max-norm of pointwise errors of the SLFV method in Definition 3.1 as

$$(4.2) \quad e_n := \sup_{\mathbf{x} \in \Omega} |\tilde{\rho}^n(\mathbf{x}) - \rho(\mathbf{x}, t_n)|.$$

Suppose there exists a constant  $C$  independent on  $k$  such that,

$$(4.3) \quad \forall n \in \mathbb{N}, \quad e_{n+1} \leq (1 + Ck)e_n + O(h^5 + k^5).$$

Then a straightforward induction and the identity  $\lim_{n \rightarrow \infty} (1 + \frac{C}{n})^n = \exp(C)$  yield

$$(4.4) \quad e_n \leq \exp(CT)e_0 + O\left(\frac{1}{k}h^5 + k^4\right) = O\left(\frac{1}{k}h^5 + k^4\right),$$

where we have assumed that the initial error is  $e_0 = O\left(\frac{1}{k}h^5 + k^4\right)$ .

For any control volume  $\mathbf{i}$ , the (cell-averaged) solution error satisfies

$$\begin{aligned} |\langle \rho \rangle_{\mathbf{i}}^n - \langle \rho(\mathbf{x}, t_n) \rangle_{\mathbf{i}}| &= |I_{\mathbf{i}}(\tilde{\rho}^n) - \langle \rho(\mathbf{x}, t_n) \rangle_{\mathbf{i}}| \\ &\leq |I_{\mathbf{i}}(\tilde{\rho}^n) - I_{\mathbf{i}}(\rho(\mathbf{x}, t_n))| + |I_{\mathbf{i}}(\rho(\mathbf{x}, t_n)) - \langle \rho(\mathbf{x}, t_n) \rangle_{\mathbf{i}}|, \end{aligned}$$

where the equality follows from (SLFV-5); in the second line, the first RHS term is a linear combination of pointwise errors at the quadrature points in cell  $\mathbf{i}$  and the second the truncation error of the quadrature formula. For any pure cell, the quadrature is performed by recursively invoking one-dimensional Gauss formulas, yielding  $|I_{\mathbf{i}}(\rho(\mathbf{x}, t_n)) - \langle \rho(\mathbf{x}, t_n) \rangle_{\mathbf{i}}| = O(h^5)$ , which also holds for an interface cell because of Lemma 4.1 and the fact of  $q = 3$  and  $\kappa = 4$  giving  $\lceil \frac{(\kappa+2)q}{2} \rceil = 9$ . Then,  $\sum_{m=1}^M \omega_{\mathbf{i},m} = 1$  and (4.4) imply

$$\begin{aligned} |\langle \rho \rangle_{\mathbf{i}}^n - \langle \rho(\mathbf{x}, t_n) \rangle_{\mathbf{i}}| &\leq \sum_{m=1}^M \omega_{\mathbf{i},m} |\tilde{\rho}^n(\mathbf{x}_{\mathbf{i},m}) - \rho(\mathbf{x}_{\mathbf{i},m}, t_n)| + O(h^5) \\ &\leq e_n \sum_{m=1}^M \omega_{\mathbf{i},m} + O(h^5) = O\left(\frac{1}{k}h^5 + k^4\right) \end{aligned}$$

and the fourth-order convergence of the SLFV method follows from  $k = O(h)$ .

We now prove the recurrence relation (4.3). Denote by  $\mathcal{T}$  and  $\mathcal{T}_k$  the exact and discrete operator, respectively, for solving the ODE system

$$(4.5) \quad \frac{d}{dt} \begin{bmatrix} \rho \\ \mathbf{x} \end{bmatrix} = \begin{bmatrix} S \\ \mathbf{u} \end{bmatrix}(\mathbf{x}, t),$$

which is the combination of (1.3) and (2.1). Accordingly, denote by  $\overleftarrow{\mathbf{x}}^* := \phi_{t_{n+1}}^{-k}(\mathbf{x})$  and  $\overleftarrow{\mathbf{x}}$  the exact and approximate preimage of  $\mathbf{x}$ , respectively.

For any quadrature point  $\mathbf{x}$  with  $\hat{\mathbf{x}} \in \Omega$ , we adopt the shorthand notation  $\mathbf{v} := [f(\hat{\mathbf{x}}), \hat{\mathbf{x}}]^\top$ ,  $\mathbf{w} := [\rho(\hat{\mathbf{x}}^*, t_n), \hat{\mathbf{x}}^*]^\top$  and deduce, from [Definition 3.1](#),

$$\begin{aligned}
 (4.6) \quad & |\tilde{\rho}^{n+1}(\mathbf{x}) - \rho(\mathbf{x}, t_{n+1})| = |\mathcal{T}_k \mathbf{v} - \mathcal{T} \mathbf{w}| \leq |\mathcal{T}_k \mathbf{v} - \mathcal{T} \mathbf{v}| + |\mathcal{T} \mathbf{v} - \mathcal{T} \mathbf{w}| \\
 & = |\mathcal{T} \mathbf{v} - \mathcal{T} \mathbf{w}| + O(k^5) \leq (1 + Ck) \|\mathbf{v} - \mathbf{w}\| + O(k^5) \\
 & = (1 + Ck) |f(\hat{\mathbf{x}}) - \rho(\hat{\mathbf{x}}^*, t_n)| + O(k^5) \leq (1 + Ck) e_n + O(h^5 + k^5),
 \end{aligned}$$

where  $f$  is the local bi-variate polynomial described in [Subsection 3.3](#). In (4.6), the first step follows from (SLFV-4), the second from the triangular inequality, the third and the fifth from the 4th-order accuracy of the RK method in  $\mathcal{T}_k$ , the fourth from [Lemma 4.2](#), and the last from

$$\begin{aligned}
 |f(\hat{\mathbf{x}}) - \rho(\hat{\mathbf{x}}^*, t_n)| & \leq |f(\hat{\mathbf{x}}) - \tilde{\rho}^n(\hat{\mathbf{x}})| + |\tilde{\rho}^n(\hat{\mathbf{x}}) - \rho(\hat{\mathbf{x}}, t_n)| + |\rho(\hat{\mathbf{x}}, t_n) - \rho(\hat{\mathbf{x}}^*, t_n)| \\
 & = |\tilde{\rho}^n(\hat{\mathbf{x}}) - \rho(\hat{\mathbf{x}}^*, t_n)| + O(h^5 + k^5) \leq e_n + O(h^5 + k^5),
 \end{aligned}$$

where the first inequality follows from the triangular inequality, the equality from the 5th-order reconstruction in space and the 4th-order accuracy of time integration, and the last inequality from (4.2).

For a quadrature point  $\mathbf{x}$  with  $\hat{\mathbf{x}} \notin \Omega$ , we calculate  $\tilde{\rho}^{n+1}(\mathbf{x})$  by (3.12). As  $k \rightarrow 0$ , the Newton iteration in [Subsection 3.2](#) must converge. Denote by  $\tilde{\mathbf{x}}$  and  $\tilde{t}$  the calculated intersection point and time, respectively, adopt the shorthand notation  $\mathbf{v}_\times := [\rho_{bc}(\tilde{\mathbf{x}}, \tilde{t}), \tilde{\mathbf{x}}]^\top$ ,  $\mathbf{w}_\times := [\rho_{bc}(\mathbf{x}^*, t^*), \mathbf{x}^*]^\top$ , and we have

$$\begin{aligned}
 (4.7) \quad & |\tilde{\rho}^{n+1}(\mathbf{x}) - \rho(\mathbf{x}, t_{n+1})| = |\mathcal{T}_k \mathbf{v}_\times - \mathcal{T} \mathbf{w}_\times| \leq |\mathcal{T}_k \mathbf{v}_\times - \mathcal{T} \mathbf{v}_\times| + |\mathcal{T} \mathbf{v}_\times - \mathcal{T} \mathbf{w}_\times| \\
 & = |\mathcal{T} \mathbf{v}_\times - \mathcal{T} \mathbf{w}_\times| + O(k^5) \leq (1 + Ck) \|\mathbf{v}_\times - \mathbf{w}_\times\| + O(k^5) = O(k^5),
 \end{aligned}$$

where the first step follows from (3.12), and the second from the triangular inequality, the third from the 4th-order accuracy of time integration, the fourth from [Lemma 4.2](#), and the last from the smoothness of  $\rho_{bc}$  and  $\|[\tilde{\mathbf{x}}, \tilde{t}]^\top - [\mathbf{x}^*, t^*]^\top\| = O(k^5)$ .

At any non-quadrature location  $\mathbf{x}$ , the numerical result of SLFV is defined as a linear combination of those at quadrature points, with the weights depending only on the Gauss quadrature formula and the local bi-variate polynomial in (SLFV-4). Thus  $|\tilde{\rho}^{n+1}(\mathbf{x}) - \rho(\mathbf{x}, t_{n+1})|$  also satisfies (4.6) or (4.7). Therefore (4.3) holds.  $\square$

In the above proof, the ODE system (4.5) numerically solved by the SLFV method is linear. Nonetheless, the analysis based on the recurrence relation (4.3) may also apply to some nonlinear problems such as the Vlasov-Poisson system; see [4].

The analysis in this section answers (Q-4).

**5. Tests.** In this section, we test the proposed SLFV method with a wide range of benchmark problems to demonstrate its high-order accuracy and good conditioning, its effectiveness for incoming penetration conditions, and its capability of handling irregular domains with arbitrarily complex topology and geometry. In [Table 1](#), we summarize various configurations of these tests, in which we employ the classical fourth-order RK method, Verner's sixth-order RK method [37] and Dormand and Prince's eighth-order RK method [25] to test the fourth-, sixth-, and eighth-order SLFV methods, respectively.

TABLE 1

Overview of test cases in [Section 5](#). The benchmark problems in the first two subsections are meant to check convergence rates of the proposed SLFV method on regular or irregular domains, for solenoidal or non-solenoidal velocity fields, and with penetration or no-penetration conditions. The test in [Subsection 5.3](#) focuses on the accuracy comparison of the SLFV method with the EL-RK-FV method by Nakao, Chen, and Qiu [24], those in [Subsection 5.4](#) demonstrate the capability of SLFV in tackling practical applications such as chaotic mixing, and those in [Subsection 5.5](#) confirm the applicability of SLFV to domains with complex topology and geometry.

Subsection	zero source term	regular domain	incoming penetration	solenoidal velocity
<a href="#">5.1</a>	yes	yes	no	yes
<a href="#">5.2</a>	no	no	yes	no
<a href="#">5.3</a>	yes	yes	yes	yes
<a href="#">5.4</a>	yes	yes	yes	yes
<a href="#">5.5</a>	yes	no	yes	yes

The  $L^p$  norm of a scalar function  $g : \Omega \rightarrow \mathbb{R}$  is defined as

$$\|g\|_p = \begin{cases} \left( \sum_{\mathcal{C}_i \subset \Omega} \|\mathcal{C}_i\| \cdot |\langle g \rangle_i|^p \right)^{\frac{1}{p}} & \text{if } p = 1, 2; \\ \max_{\mathcal{C}_i \subset \Omega} |\langle g \rangle_i| & \text{if } p = \infty, \end{cases}$$

where the cut cell  $\mathcal{C}_i$  and the cell average  $\langle g \rangle_i$  are given in [\(3.2\)](#) and [\(3.3\)](#), respectively.

Denote by  $\rho_h$  the numerical solution on a grid of size  $h$  and  $r$  the grid refinement ratio. If the analytic solution  $\rho$  is available, the error of  $\rho_h$  is measured by  $E_h := \rho_h - \rho$ ; otherwise Richardson extrapolation is employed, i.e.,  $E_h := \rho_h - \rho_{\frac{h}{r}}$ . Then the convergence rate is given by  $\kappa := \log_r \frac{\|E_{rh}\|_p}{\|E_h\|_p}$ .

**5.1. A solenoidal velocity field on a regular no-penetration domain.** On the unit box  $\Omega = (0, 1)^2$ , we set  $S = 0$  and

$$\mathbf{u}(x, y, t) = \begin{pmatrix} -\sin^2(\pi x) \sin(\pi y) \cos(\pi y) \\ \sin(\pi x) \cos(\pi x) \sin^2(\pi y) \end{pmatrix} \sin(t)$$

in [\(1.1\)](#) and choose the initial and boundary conditions of  $\rho$  to be

$$\rho_{\text{init}}(x, y) = \rho_{\text{bc}}(x, y, t) = x + y.$$

We solve the advection equation [\(1.1\)](#) to the final time  $T = 1$  with the time step size as  $k = 8h$ . Since no analytic solution is available, we calculate errors and convergence rates of SLFV via Richardson extrapolation and present them in [Table 2](#), which clearly demonstrate the fourth- and sixth-order convergence rates of SLFV.

Due to  $S = 0$  and  $\nabla \cdot \mathbf{u} = 0$ , [\(1.1\)](#) is equivalent to the scalar conservation law  $\frac{\partial \rho}{\partial t} + \nabla \cdot (\rho \mathbf{u}) = 0$ . We define the relative error of mass conservation as

$$(5.1) \quad E_{\text{mass}}^{\text{rel}}(t_n) := \frac{\iint_{\Omega} \rho(x, y, t_n) \, dx dy - \iint_{\Omega} \rho_{\text{init}}(x, y) \, dx dy}{\iint_{\Omega} \rho_{\text{init}}(x, y) \, dx dy}.$$

The evolution of  $E_{\text{mass}}^{\text{rel}}$  for the fourth-order SLFV method with  $h = \frac{1}{256}$  is shown in [Figure 8](#), where  $\max_{t_n} |E_{\text{mass}}^{\text{rel}}(t_n)|$  is about  $5 \times 10^{-11}$ , which is much smaller than



TABLE 2

Errors and convergence rates of the  $\kappa$ -th order SLFV method for the test in [Subsection 5.1](#). The errors are calculated by Richardson extrapolation.

$\kappa$		$\frac{1}{32}$	$\frac{1}{64}$	rate	$\frac{1}{64}$	$\frac{1}{128}$	rate	$\frac{1}{128}$	$\frac{1}{256}$	rate	$\frac{1}{256}$	$\frac{1}{512}$
4	$L^\infty$	1.16e-04	3.98	7.36e-06	4.01	4.57e-07	4.09	2.68e-08				
	$L^1$	2.95e-05	4.01	1.83e-06	4.02	1.13e-07	4.09	6.63e-09				
	$L^2$	4.65e-05	4.01	2.89e-06	4.01	1.79e-07	4.09	1.05e-08				
6	$L^\infty$	1.44e-07	5.68	2.81e-09	5.77	5.15e-11	5.93	8.43e-13				
	$L^1$	3.08e-08	5.84	5.37e-10	5.99	8.42e-12	6.04	1.28e-13				
	$L^2$	4.65e-08	5.83	8.19e-10	5.91	1.36e-11	5.98	2.16e-13				

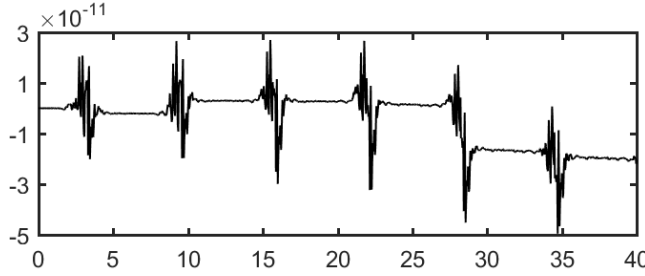


FIG. 8. The evolution of the relative error of mass conservation for the fourth-order SLFV method in solving the test in [Subsection 5.1](#) on a grid of  $h = \frac{1}{256}$  within the time interval  $[0, 40]$ . The horizontal and vertical axes represent the time and the relative error in (5.1), respectively.

$4.57 \times 10^{-7}$ , the  $L^\infty$ -norm of the solution error in [Table 2](#). Since the error of mass conservation is always smaller than the solution error, a high-order method tends to accurately conserve the total mass.

### 5.2. A non-solenoidal velocity field on an irregular penetration domain.

In this test we set  $\Omega$  to a trapezoid with its vertices at  $(0.5, 0)$ ,  $(2, 0)$ ,  $(2, 2)$ , and  $(0, 2)$ . The velocity and the exact solution of  $\rho$  are

$$\mathbf{u}(x, y, t) = \begin{pmatrix} x^2 + y^2 + t \\ x + y - 2t \end{pmatrix}; \quad \rho(x, y, t) = \sin(x + y + t),$$

for which the advection equation (1.1) is closed by the source term

$$S = \cos(x + y + t)(1 + x^2 + y^2 + x + y - t).$$

We solve (1.1) to the final time  $T = 1$  with  $k = 8h$ . Errors and convergence rates are presented in [Table 3](#), confirming the fourth- and sixth-order convergence rates of SLFV over the irregular domain.

**5.3. Solid-body rotation on a regular periodic penetration domain.** On the domain  $\Omega = (-\pi, \pi)^2$ , we set the velocity and the exact solution of  $\rho$  to be

$$\mathbf{u}(x, y, t) = \begin{pmatrix} -y \\ x \end{pmatrix}; \quad \rho(x, y, t) = \exp(-3(x^2 + y^2)),$$

for which the equation (1.1) is closed with the zero source term  $S = 0$ . The boundary conditions of  $\rho$  are set to be periodic and the final time is  $T = 0.5$ . This test is exactly

TABLE 3  
Errors and convergence rates of the  $\kappa$ -th order SLFV method for the test in [Subsection 5.2](#).

$\kappa$		$h = \frac{1}{64}$	rate	$h = \frac{1}{128}$	rate	$h = \frac{1}{256}$	rate	$h = \frac{1}{512}$
4	$L^\infty$	1.07e-03	4.14	6.03e-05	4.03	3.68e-06	4.01	2.29e-07
	$L^1$	7.21e-04	4.05	4.35e-05	4.02	2.68e-06	4.01	1.67e-07
	$L^2$	6.55e-04	4.10	3.81e-05	4.03	2.33e-06	4.01	1.45e-07
6	$L^\infty$	1.79e-05	5.45	4.08e-07	5.86	7.01e-09	5.96	1.13e-10
	$L^1$	2.34e-06	5.68	4.57e-08	5.90	7.68e-10	5.97	1.22e-11
	$L^2$	2.91e-06	5.43	6.74e-08	5.84	1.17e-09	5.96	1.89e-11

TABLE 4  
Errors and convergence rates of the  $\kappa$ -th order SLFV method and the EL-RK-FV method by Nakao, Chen, and Qiu [\[24\]](#) for the test in [Subsection 5.3](#) with  $CFL = \frac{k(\max |u| + \max |v|)}{h}$ .

CFL		$h = \frac{1}{100}$	rate	$h = \frac{1}{200}$	rate	$h = \frac{1}{300}$	rate	$h = \frac{1}{400}$
0.95	The EL-RK-FV method by Nakao, Chen, and Qiu <a href="#">[24]</a>							
	$L^\infty$	8.95e-05	6.85	7.74e-07	5.00	1.02e-07	4.99	2.43e-08
	$L^1$	1.05e-04	6.60	1.08e-06	5.06	1.39e-07	4.99	3.32e-08
	$L^2$	4.66e-05	6.25	6.13e-07	4.99	8.12e-08	4.99	1.93e-08
	Our fourth-order SLFV method							
	$L^\infty$	3.55e-05	4.58	1.49e-06	4.15	2.76e-07	5.07	6.42e-08
	$L^1$	1.02e-06	4.85	3.55e-08	4.87	4.92e-09	4.49	1.35e-09
	$L^2$	3.46e-06	4.79	1.25e-07	4.91	1.71e-08	4.57	4.58e-09
	Our sixth-order SLFV method							
	$L^\infty$	1.83e-06	6.19	2.50e-08	7.42	1.24e-09	6.60	1.85e-10
	$L^1$	3.40e-08	6.63	3.43e-10	7.03	1.99e-11	6.36	3.18e-12
	$L^2$	1.22e-07	6.54	1.31e-09	7.28	6.83e-11	6.29	1.12e-11
	Our eighth-order SLFV method							
	$L^\infty$	5.60e-08	8.50	1.55e-10	8.65	4.63e-12	7.95	4.70e-13
	$L^1$	1.32e-09	8.85	2.86e-12	9.01	7.39e-14	7.14	9.47e-15
	$L^2$	4.61e-09	8.77	1.06e-11	8.92	2.84e-13	7.19	3.59e-14
8	The EL-RK-FV method by Nakao, Chen, and Qiu <a href="#">[24]</a>							
	$L^\infty$	6.82e-05	7.16	4.77e-07	5.03	6.19e-08	5.00	1.47e-08
	$L^1$	4.95e-05	6.68	4.84e-07	5.08	6.17e-08	4.99	1.47e-08
	$L^2$	2.46e-05	6.39	2.92e-07	4.99	3.86e-08	4.88	9.22e-09
	Our fourth-order SLFV method							
	$L^\infty$	3.03e-05	4.85	1.05e-06	5.05	1.36e-07	5.13	3.10e-08
	$L^1$	4.79e-07	4.72	1.81e-08	4.88	2.51e-09	5.31	5.44e-10
	$L^2$	2.03e-06	4.77	7.42e-08	4.87	1.03e-08	5.23	2.29e-09
	Our sixth-order SLFV method							
	$L^\infty$	8.66e-07	6.88	7.33e-09	6.93	4.41e-10	6.82	6.20e-11
	$L^1$	1.89e-08	7.02	1.46e-10	6.90	8.89e-12	6.78	1.26e-12
	$L^2$	7.77e-08	6.96	6.23e-10	6.97	3.69e-11	6.81	5.19e-12
	Our eighth-order SLFV method							
	$L^\infty$	4.67e-08	8.75	1.09e-10	8.85	3.00e-12	8.31	2.75e-13
	$L^1$	7.59e-10	8.96	1.53e-12	8.51	4.84e-14	7.11	6.26e-15
	$L^2$	3.20e-09	8.90	6.71e-12	8.71	1.96e-13	8.22	1.85e-14

TABLE 5

CPU time (in seconds) of the  $\kappa$ -th order SLFV method for solving the test problem in [Subsection 5.3](#) with  $CFL = \frac{k(\max |u| + \max |v|)}{h}$  on an Intel Core i7-7500U CPU @ 2.70GHz.

CFL	$\kappa$	$h = \frac{1}{100}$	rate	$h = \frac{1}{200}$	rate	$h = \frac{1}{300}$	rate	$h = \frac{1}{400}$
0.95	4	16.77	3.00	133.96	3.00	455.94	2.98	1075.50
	6	81.14	2.99	646.28	3.00	2176.83	2.95	5091.73
	8	118.39	3.01	955.75	3.00	3227.25	2.98	7600.98
8	4	2.04	2.99	16.19	2.99	54.42	2.96	127.42
	6	9.66	2.99	76.72	3.00	259.04	2.97	608.44
	8	14.89	3.01	119.56	3.03	408.68	2.95	955.20

TABLE 6

Errors and convergence rates of the  $\kappa$ -th order SLFV method for the chaotic mixing test in [Subsection 5.4](#) with  $T = 0.1$  and  $k = 0.4h$ . The errors are calculated by Richardson extrapolation.

$\kappa$		$\frac{1}{32}$	$\frac{1}{64}$	rate	$\frac{1}{64}$	$\frac{1}{128}$	rate	$\frac{1}{128}$	$\frac{1}{256}$	rate	$\frac{1}{256}$	$\frac{1}{512}$
4	$L^\infty$	3.18e-04	3.53	2.75e-05	3.68	2.14e-06	3.94	1.40e-07				
	$L^1$	5.24e-05	4.01	3.26e-06	3.90	2.18e-07	3.97	1.39e-08				
	$L^2$	7.92e-05	3.93	5.20e-06	3.90	3.48e-07	3.95	2.24e-08				
6	$L^\infty$	6.25e-05	5.68	1.22e-06	5.65	2.42e-08	5.93	3.97e-10				
	$L^1$	9.09e-06	5.90	1.52e-07	6.01	2.36e-09	5.74	4.42e-11				
	$L^2$	1.42e-05	5.86	2.43e-07	5.97	3.89e-09	5.87	6.67e-11				

the same as that in [\[24, Example 4.5\]](#) so that it is meaningful to compare our SLFV method to the EL-RK-FV method by Nakao, Chen, and Qiu [\[24\]](#).

Errors and convergence rates of these two methods are presented in [Table 4](#), where the fourth-, sixth-, and eighth-order convergence rates of SLFV are demonstrated for small and large CFL numbers. While errors of the fourth-order SLFV are close to those of EL-RK-FV, those of the sixth-order and eighth-order SLFV methods are much smaller, confirming the advantage of higher-order SLFV methods. For example, on the finest grid, the eighth-order SLFV is more accurate than EL-RK-FV by five orders of magnitude. The  $L^1$ -norm being close to machine precision also indicates an excellent conditioning of SLFV.

It appears that the extension of EL-RK-FV to the sixth and eighth orders involves splitting techniques that are more complex than that of the fourth-order EL-RK-FV. In contrast, the extension of the fourth-order SLFV to higher orders is as simple as changing values of the input parameters; see [Theorem 4.3](#) and its proof.

The CPU time of the SLFV method for generating results in [Table 4](#) is reported in [Table 5](#), where the increase rate of CPU time is very close to 3, demonstrating the *optimal* complexity of SLFV that the CPU time is linearly proportional to the number of control volumes at each time step. In addition, these rates also imply that the expense of complex treatments on an  $O(\frac{1}{h})$  number of cells near the domain boundary is dominated by that of simple algorithmic steps on an  $O(\frac{1}{h^2})$  number of cells away from the boundary.

**5.4. Transient chaotic mixing on a regular penetration domain.** One realworld phenomenon that is challenging to numerical methods for the advection equation is the transient chaotic fluid mixing problem, of which the solution may evolve to be highly complex even for simple initial conditions and smooth velocity

TABLE 7

Errors and convergence rates of the  $\kappa$ -th order SLFV method for the chaotic mixing test in Subsection 5.5 with  $T = 0.1$  and  $k = 0.4h$ . The errors are calculated by Richardson extrapolation.

$\kappa$		$\frac{1}{256}$	$\frac{1}{512}$	rate	$\frac{1}{512}$	$\frac{1}{1024}$	rate	$\frac{1}{1024}$	$\frac{1}{2048}$
4	$L^\infty$	6.14e-07	3.70	4.73e-08	3.98	3.00e-09			
	$L^1$	8.82e-08	3.90	5.92e-09	4.05	3.58e-10			
	$L^2$	1.36e-07	3.88	9.26e-09	4.05	5.60e-10			
6	$L^\infty$	9.96e-09	5.80	1.79e-10	6.09	2.62e-12			
	$L^1$	1.26e-09	5.75	2.34e-11	5.92	3.88e-13			
	$L^2$	1.84e-09	5.68	3.58e-11	5.94	5.84e-13			

fields. Such an example is studied in [22], where the domain is a unit box  $\Omega = (0, 1)^2$ , the source term in (1.1) is set to  $S = 0$ , the initial condition is  $\rho_{\text{init}}(x, y) = \sin(2\pi y)$ , the boundary condition of  $\rho$  is periodic, and the velocity field<sup>1</sup> is

$$(5.2) \quad \begin{cases} \mathbf{u}(x, y, t) = \alpha_1(t)\mathbf{u}_1(x, y) + \alpha_2(t)\mathbf{u}_2(x, y), \\ \mathbf{u}_1(x, y) = \begin{pmatrix} -\sin(2\pi x) \cos(2\pi y) \\ \cos(2\pi x) \sin(2\pi y) \end{pmatrix}, \\ \mathbf{u}_2(x, y) = \begin{pmatrix} -\sin(2\pi(x - 0.25)) \cos(2\pi(y - 0.25)) \\ \cos(2\pi(x - 0.25)) \sin(2\pi(y - 0.25)) \end{pmatrix}, \end{cases}$$

where the coefficients  $\alpha_1(t)$  and  $\alpha_2(t)$  are cubic splines fitted from characteristic points of the curves in [22, Figure 2(b)].

Errors and convergence rates of SLFV at  $T = 0.1$  with  $k = 0.4h$  are listed in Table 6, clearly demonstrating the fourth- and sixth-order convergences rates. In Figure 9, we present snapshots of the solution at six time instances, of which the patterns and structures are visually indistinguishable from those in [22, Figure 4].

**5.5. Transient chaotic mixing on a complex penetration domain.** The test in Subsection 5.4 is made even more challenging by changing the domain  $\Omega$  from the unit box to a panda adapted from [41, Figure 10]; see Figure 10. The complex topology and geometry present serious challenges for Boolean algorithms in cutting cells with the irregular boundary  $\partial\Omega$  and for the Newton iteration in intersecting pathlines with the domain boundary.

While the velocity on  $\partial\Omega$  is still given by (5.2), the boundary condition of  $\rho$  is obtained from the computational results on the regular unit box with the same grid size  $h$  via a sufficiently accurate polynomial interpolation. All other parameters of this test are exactly the same as those in Subsection 5.4. Consequently, we expect that solutions on the panda match very well with those on the unit box, as if solutions on the panda were “cut” from those on the regular domain by the shape of the panda.

Note that values of  $\rho$  are not needed for all points on  $\partial\Omega$ , since the steps of SLFV in Definition 3.1 only concern those at the intersections of pathlines to the boundary of panda. This highlights an advantage of SLFV as being worry free about the type of the boundary condition (1.1c).

In Figure 10, we present snapshots of the solution in the same manner and at the same instants with those in Figure 9; any two corresponding subplots are visually

<sup>1</sup>In [22], the second component of  $\mathbf{u}_1$  is  $-\cos(2\pi x) \sin(2\pi y)$ , of which the minus sign appears to be incorrect since the solutions of SLFV with (5.2) agree very well with figures in [22] but those with the incorrect minus sign differ largely with results in [22].

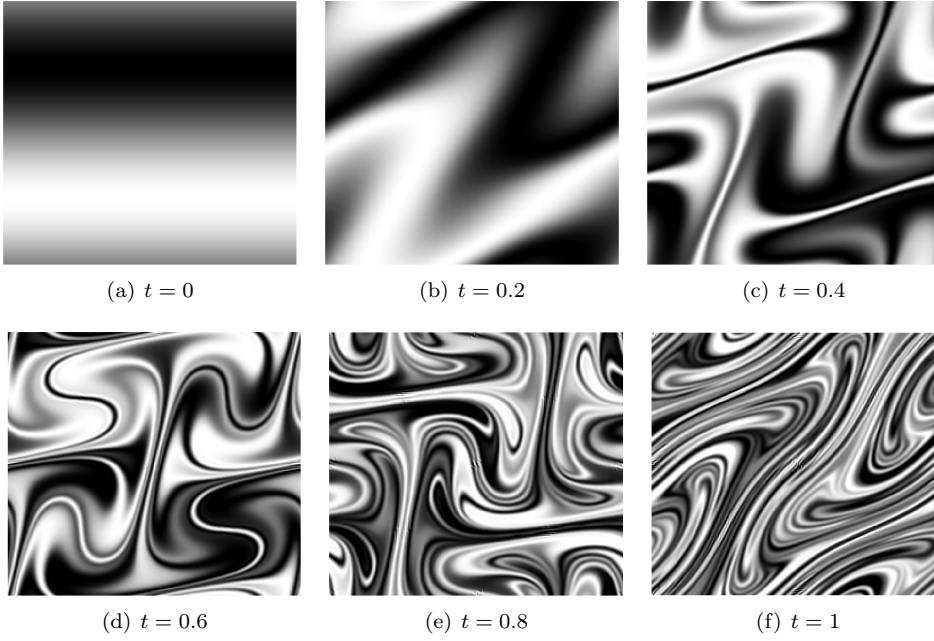


FIG. 9. Results of the SLFV method for the chaotic mixing test in [Subsection 5.4](#) on a regular domain with  $h = \frac{1}{256}$ . The lightest color corresponds to the value of 1 and the darkest color corresponds to the value of  $-1$ .

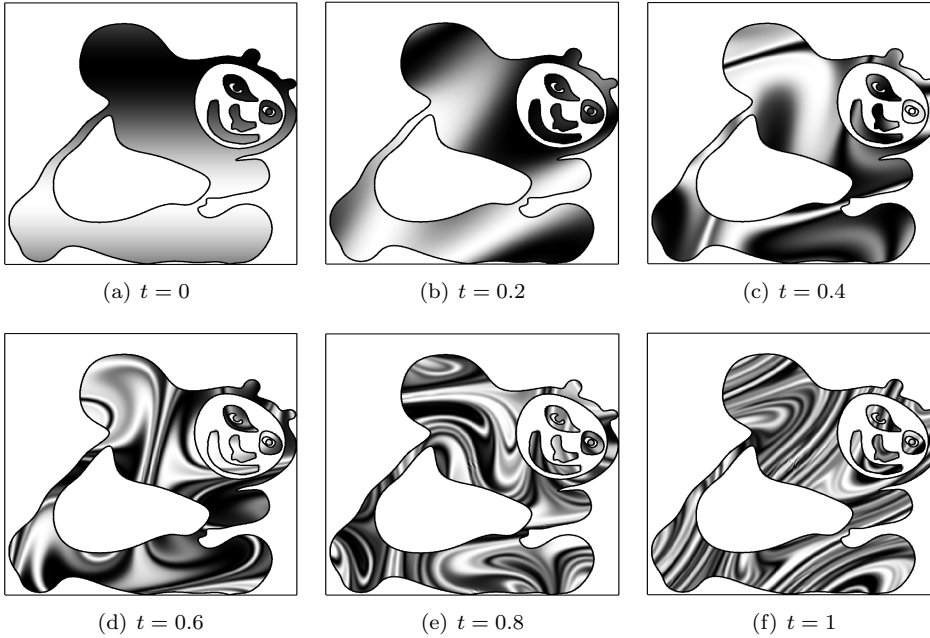


FIG. 10. Results of the SLFV method for the chaotic mixing test in [Subsection 5.5](#) on a complex irregular domain with  $h = \frac{1}{256}$ . The lightest color corresponds to the value of 1 and the darkest color corresponds to the value of  $-1$ . In each snapshot, the solution over the panda is supposed to be the same as that in the corresponding subplot in [Figure 9](#).

indistinguishable over the panda region, which indicates an accurate handling of the complex domain. As more quantitative evidences, errors and convergence rates of the solution  $\rho$  at  $T = 0.1$  are presented in Table 7, clearly demonstrating the fourth- and sixth-order convergence rates of our SLFV method over this highly irregular domain.

**6. Conclusion.** We have proposed fourth- and higher-order SLFV methods for solving the two-dimensional advection equation on both regular and irregular domains with periodic and incoming penetration conditions. The main components of SLFV are the Yin sets for representing domains with arbitrarily complex topology and geometry, Gauss quadrature formulas on quadrilaterals/triangles, and a Newton iteration algorithm for intersecting a pathline with the domain boundary. The orthogonality of these components furnishes flexibility, user friendliness, and the ease of implementation. Results of various numerical tests demonstrate the effectiveness of SLFV, its excellent conditioning, and its high-order convergence rates both in time and in space.

To prove the high-order convergence rates of SLFV, we have assumed the smoothness of the solution of the advection equation. If the source term in (1.1a) vanishes and the initial condition in (1.1b) contains discontinuities, the high-order convergence rates can be maintained by coupling this work to a high-order interface tracking method, such as the MARS method in [40], which tracks the loci of discontinuity on a one-dimensional CW-complex. We will report this extension in a future paper.

It should be straightforward to extend the SLFV method to solving the advection equation (1.1) on moving domains. The key distinction lies in the treatment of incoming penetration conditions: instead of computing the intersection point  $\mathbf{x}^*$  of the particle pathline with the fixed domain boundary in  $\mathbb{R}^2$ , for moving boundaries we determine the space-time intersection point  $(\mathbf{x}^*, t^*)$  in the extended phase space  $\mathbb{R}^2 \times \mathbb{R}$  and set the value of the corresponding quadrature point to be the solution of (1.1a) whose initial condition  $\rho(\mathbf{x}^*, 0)$  is the boundary condition at  $(\mathbf{x}^*, t^*)$ .

We also plan to extend the SLFV method to the nonlinear advection equation and validate its efficacy through the guiding-center model [12, 13]. Subsequently, we will couple the SLFV method with high-order methods for incompressible Navier-Stokes equations [39, 21] to form a more sophisticated solver, which could be useful in studying physical processes governed by the Boussinesq equations.

**Acknowledgments.** We are grateful to two anonymous referees for their insightful comments and suggestions. We also thank helpful comments from Shuang Hu and Chenhao Ye, graduate students at the school of mathematical sciences in Zhejiang University.

## REFERENCES

- [1] E. ABREU, W. LAMBERT, J. PEREZ, AND A. SANTO, *A new finite volume approach for transport models and related applications with balancing source terms*, Mathematics and Computers in Simulation, 137 (2017), pp. 2–28.
- [2] M. L. BÉGUÉ, A. GHIZZO, P. BERTRAND, E. SONNENDRÜCKER, AND O. COULAUD, *Two-dimensional semi-Lagrangian Vlasov simulations of laser-plasma interaction in the relativistic regime*, Journal of Plasma Physics, 62 (1999), pp. 367–388.
- [3] F. BENKHALDOUN, S. SARI, AND M. SEID, *A family of finite volume Eulerian-Lagrangian methods for two-dimensional conservation laws*, Journal of Computational and Applied Mathematics, 285 (2015), pp. 181–202.
- [4] N. BESSE AND M. MEHRENBARGER, *Convergence of classes of high-order semi-Lagrangian schemes for the Vlasov-Poisson system*, Mathematics of Computation, 77 (2008), pp. 93–123.
- [5] N. BESSE AND E. SONNENDRÜCKER, *Semi-Lagrangian schemes for the Vlasov equation on an*



- unstructured mesh of phase space*, Journal of Computational Physics, 191 (2003), pp. 341–376.
- [6] J. A. CARRILLO AND F. VECIL, *Nonoscillatory interpolation methods applied to Vlasov-based models*, SIAM Journal on Scientific Computing, 29 (2007), pp. 1179–1206.
  - [7] J. CHEN, *Adaptive order WENO reconstructions for the semi-Lagrangian finite difference scheme for advection problem*, Communications in Computational Physics, 30 (2021).
  - [8] Y. CHEN, W. GUO, AND X. ZHONG, *A learned conservative semi-Lagrangian finite volume scheme for transport simulations*, Journal of Computational Physics, 490 (2023), p. 112329.
  - [9] P. COLELLA AND P. R. WOODWARD, *The piecewise parabolic method (PPM) for gas-dynamical simulations*, Journal of Computational Physics, 54 (1984), pp. 174–201.
  - [10] N. CROUSEILLES, P. GLANC, S. A. HIRSTOAGA, E. MADAULE, M. MEHRENBARGER, AND J. PÉTRI, *A new fully two-dimensional conservative semi-Lagrangian method: applications on polar grids, from diocotron instability to ITG turbulence*, The European Physical Journal D, 68 (2014), pp. 1–10.
  - [11] N. CROUSEILLES, G. LATU, AND E. SONNENDRÜCKER, *Hermite spline interpolation on patches for parallelly solving the Vlasov-Poisson equation*, International Journal of Applied Mathematics and Computer Science, 17 (2007), pp. 335–349.
  - [12] N. CROUSEILLES, M. MEHRENBARGER, AND E. SONNENDRÜCKER, *Conservative semi-Lagrangian schemes for Vlasov equations*, Journal of Computational Physics, 229 (2010), pp. 1927–1953.
  - [13] N. CROUSEILLES, M. MEHRENBARGER, AND F. VECIL, *A discontinuous Galerkin semi-Lagrangian solver for the guiding-center problem*. 2012, <https://inria.hal.science/hal-00717155>.
  - [14] L. EINKEMMER AND A. MORIGGL, *A semi-Lagrangian discontinuous Galerkin method for drift-kinetic simulations on GPUs*, SIAM Journal on Scientific Computing, 46 (2024), pp. B33–B55.
  - [15] D. HU, K. LIANG, L. YING, S. LI, AND Q. ZHANG, *ARMS: Adding and removing markers on splines for high-order general interface tracking under the MARS framework*, Journal of Computational Physics, 521 (2025), p. 113574.
  - [16] C.-S. HUANG, T. ARBOGAST, AND J. QIU, *An Eulerian-Lagrangian WENO finite volume scheme for advection problems*, Journal of Computational Physics, 231 (2012), pp. 4028–4052.
  - [17] F. HUOT, A. GHIZZO, P. BERTRAND, E. SONNENDRÜCKER, AND O. COULAUD, *Instability of the time splitting scheme for the one-dimensional and relativistic Vlasov-Maxwell system*, Journal of Computational Physics, 185 (2003), pp. 512–531.
  - [18] G.-S. JIANG AND C.-W. SHU, *Efficient implementation of weighted ENO schemes*, Journal of Computational Physics, 126 (1996), pp. 202–228.
  - [19] P. H. LAURITZEN, R. D. NAIR, AND P. A. ULLRICH, *A conservative semi-Lagrangian multi-tracer transport scheme (CSLAM) on the cubed-sphere grid*, Journal of Computational Physics, 229 (2010), pp. 1401–1424.
  - [20] L. LI, J.-M. QIU, AND G. RUSSO, *A high-order semi-Lagrangian finite difference method for nonlinear Vlasov and BGK models*, Communications on Applied Mathematics and Computation, 5 (2023), pp. 170–198.
  - [21] Y. LI, X. WU, J. YAN, J. YANG, Q. ZHANG, AND S. ZHAO, *GePUP-ES: High-order energy-stable projection methods for the incompressible Navier-Stokes equations with no-slip conditions*, Under Review, (2024), <https://arxiv.org/abs/2409.11255>.
  - [22] G. MATHEW, I. MEZIĆ, S. GRIVOPOULOS, U. VAIDYA, AND L. PETZOLD, *Optimal control of mixing in Stokes fluid flows*, Journal of Fluid Mechanics, 580 (2007), pp. 261–281.
  - [23] A. R. MOHEBALHOJEH AND D. G. DRITSCHER, *The diabatic contour-advective semi-Lagrangian algorithms for the spherical shallow water equations*, Monthly Weather Review, 137 (2009), pp. 2979–2994.
  - [24] J. NAKAO, J. CHEN, AND J.-M. QIU, *An Eulerian-Lagrangian Runge-Kutta finite volume (EL-RK-FV) method for solving convection and convection-diffusion equations*, Journal of Computational Physics, 470 (2022), p. 111589.
  - [25] P. J. PRINCE AND J. R. DORMAND, *High order embedded Runge-Kutta formulae*, Journal of Computational and Applied Mathematics, 7 (1981), pp. 67–75.
  - [26] J.-M. QIU AND A. CHRISTLIEB, *A conservative high order semi-Lagrangian WENO method for the Vlasov equation*, Journal of Computational Physics, 229 (2010), pp. 1130–1149.
  - [27] J.-M. QIU AND C.-W. SHU, *Conservative high order semi-Lagrangian finite difference WENO methods for advection in incompressible flow*, Journal of Computational Physics, 230 (2011), pp. 863–889.
  - [28] J.-M. QIU AND C.-W. SHU, *Positivity preserving semi-Lagrangian discontinuous Galerkin for-*

- mulation: theoretical analysis and application to the Vlasov–Poisson system*, Journal of Computational Physics, 230 (2011), pp. 8386–8409.
- [29] A. ROBERT, *A stable numerical integration scheme for the primitive meteorological equations*, Atmosphere-Ocean, 19 (1981), pp. 35–46.
  - [30] C.-W. SHU, *High order weighted essentially nonoscillatory schemes for convection dominated problems*, SIAM Review, 51 (2009), pp. 82–126.
  - [31] C.-W. SHU, *Essentially non-oscillatory and weighted essentially non-oscillatory schemes*, Acta Numerica, 29 (2020), pp. 701–762.
  - [32] P. K. SMOLARKIEWICZ AND J. A. PUDYKIEWICZ, *A class of semi-Lagrangian approximations for fluids*, Journal of Atmospheric Sciences, 49 (1992), pp. 2082–2096.
  - [33] E. SONNENDRÜCKER, J. ROCHE, P. BERTRAND, AND A. GHIZZO, *The semi-Lagrangian method for the numerical resolution of the Vlasov equation*, Journal of Computational Physics, 149 (1999), pp. 201–220.
  - [34] A. STANFORTH AND J. CÔTÉ, *Semi-Lagrangian integration schemes for atmospheric models—A review*, Monthly Weather Review, 119 (1991), pp. 2206–2223.
  - [35] B. SZABÓ AND I. BABUŠKA, *Finite element analysis: method, verification and validation*, John Wiley & Sons, 2021.
  - [36] H. TAKEWAKI, A. NISHIGUCHI, AND T. YABE, *Cubic interpolated pseudo-particle method (CIP) for solving hyperbolic-type equations*, Journal of Computational Physics, 61 (1985), pp. 261–268.
  - [37] J. H. VERNER, *Explicit Runge–Kutta methods with estimates of the local truncation error*, SIAM Journal on Numerical Analysis, 15 (1978), pp. 772–790.
  - [38] T. XIONG, G. RUSSO, AND J.-M. QIU, *Conservative multi-dimensional semi-Lagrangian finite difference scheme: stability and applications to the kinetic and fluid simulations*, Journal of Scientific Computing, 79 (2019), pp. 1241–1270.
  - [39] Q. ZHANG, *GePUP: Generic projection and unconstrained PPE for fourth-order solutions of the incompressible Navier–Stokes equations with no-slip boundary conditions*, Journal of Scientific Computing, 67 (2016), pp. 1134–1180.
  - [40] Q. ZHANG, *Fourth- and higher-order interface tracking via mapping and adjusting regular semianalytic sets represented by cubic splines*, SIAM Journal on Scientific Computing, 40 (2018), pp. A3755–A3788.
  - [41] Q. ZHANG AND Z. LI, *Boolean algebra of two-dimensional continua with arbitrarily complex topology*, Mathematics of Computation, 89 (2020), pp. 2333–2364.
  - [42] Q. ZHANG, Y. ZHU, AND Z. LI, *An AI-aided algorithm for multivariate polynomial reconstruction on Cartesian grids and the PLG finite difference method*, Journal of Scientific Computing, 101 (2024), p. 66.
  - [43] N. ZHENG, X. CAI, J.-M. QIU, AND J. QIU, *A fourth-order conservative semi-Lagrangian finite volume WENO scheme without operator splitting for kinetic and fluid simulations*, Computer Methods in Applied Mechanics and Engineering, 395 (2022), p. 114973.